# Slope, grain size, and roughness controls on dry sediment transport and storage on steep hillslopes

**Roman A. DiBiase[1], Michael P. Lamb[2], Vamsi Ganti[3], Adam M. Booth[4]**

[1]Department of Geosciences, Pennsylvania State University, University Park, PA, USA.

[2]Division of Geological and Planetary Sciences, California Institute of Technology, Pasadena, CA, USA.

[3]Department of Earth Science and Engineering, Imperial College London, South Kensington Campus, London, UK.

[4]Department of Geology, Portland State University, Portland, OR, USA.

Corresponding Author: Roman A. DiBiase (rdibiase@psu.edu)

**Abstract**

Existing hillslope sediment transport models developed for low-relief, soil-mantled landscapes are poorly suited to explain the coupling between steep rocky hillslopes and headwater channels. Here, we address this knowledge gap using a series of field and numerical experiments to inform a particle-based model of sediment transport by dry ravel – a mechanism of granular transport characteristic of steep hillslopes. We find that particle travel distance increases as a function of the ratio of particle diameter to fine-scale (<1 m) topographic roughness, in agreement with prior laboratory and field experiments. Contrary to models that assume a fixed critical slope, the particle-based model predicts a broad transition as hillslopes steepen from grain-scale to hillslope-scale mean particle travel distances, which we define as local or purely nonlocal transport, respectively, due to the trapping of sediment on slopes more than three-fold steeper than the average friction slope. This transition is further broadened by higher macro-scale (>1 m) topographic variability associated with rocky landscapes. Applying a 2D dry-ravel-routing model to lidar-derived surface topography, we show how spatial patterns of local and nonlocal transport control connectivity between hillslopes and steep headwater channels that generate debris flows through failure of ravel filled channels following wildfire. Our results corroborate field observations of a patchy transition from soil-mantled to bedrock landscapes and suggest that there is a dynamic interplay between sediment storage, roughness, grain sorting, and transport even on hillslopes that well-exceed the angle of repose.

**1 Introduction**

Hillslopes at or near the threshold for slope stability dominate the areal extent of rapidly uplifting mountain ranges [*Burbank et al.*, 1996; *Montgomery and Brandon*, 2002] and pose a significant hazard to nearby communities [*Petley*, 2012]. Additionally, the coupling between steep rocky hillslopes and headwater channels is critical for assessing debris flow hazards following wildfire or other disturbance [e.g., *Cannon et al.*, 2010]. Hillslope sediment flux in such settings is highly sensitive to external forcing (e.g., storms, earthquakes, wildfire) and is typically shaped by stochastic transport processes [*Benda and Dunne*, 1997; *Gabet and Dunne*, 2003], making it challenging to develop and test mechanistic models of erosion and sediment transport in steep landscapes.

Existing approaches to modeling steep hillslopes typically follow from some variant of the threshold hillslope model, whereby sediment flux increases nonlinearly towards a critical angle representative of a strength limitation of either soil [e.g., *Roering et al.*, 1999] or bedrock [e.g., *Burbank et al.*, 1996]. These models describe well the morphology of steep, soil-mantled landscapes [*Roering*, 2008], the observation of a nonlinear increase in erosion rates with increasing slope angle [*Ouimet et al.*, 2009; *DiBiase et al.*, 2010], and the limits of hillslope relief [*Schmidt and Montgomery*, 1995]. However, as commonly implemented, the threshold model predicts an abrupt transition from soil-mantled to bedrock hillslopes as rock uplift rates exceed the rate of soil production from bedrock [e.g., *Tucker and Hancock*, 2010], with the implication that soil residence times and thus hillslope chemical weathering tends to zero [*Ferrier and Kirchner*, 2008; *Hilley et al.*, 2010]. In contrast to these predictions, field observations indicate that the transition to bare-bedrock hillslopes is gradual and steep hillslopes often comprise a patchwork of exposed rock, soil, and loose sediment trapped behind vegetation or topographic roughness [*Norton et al.*, 2010; *DiBiase et al.*, 2012; *Heimsath et al.*, 2012; *DiBiase and Lamb*, 2013; *Milodowski et al.*, 2015]. Thus, there is a

need for new models of sediment transport and soil residence time to explain the stability of patchy soils in steep landscapes and describe sediment flux on steep, rocky hillslopes over a wide range of timescales.

Recent work focused on steep hillslope processes has highlighted the shortcomings of locality assumptions in traditional continuum-based models of soil transport where sediment flux is determined solely from local topography within a representative elementary volume [*Foufoula-Georgiou et al.*, 2010; *Furbish and Roering*, 2013]. For hillslope processes, the maximum size of a reasonable representative elementary volume is ultimately set by hillslope length. On steep slopes particles may travel distances that span from grain scale to hillslope scale, such that a separation of scales between a reasonable representative elementary volume, transport distance, and system size is unlikely. Thus, the nature of the probability distribution of travel distances and the full particle path history are necessary to describe sediment flux [*Schumer et al.*, 2009; *Foufoula-Georgiou et al.*, 2010; *Furbish and Roering*, 2013]. Accounting for such "nonlocal" transport effects requires either the development of nonlocal constitutive laws using fractional derivatives [*Schumer et al.*, 2009; *Foufoula-Georgiou et al.*, 2010], or a particle-based statistical framework [*Kirkby and Statham*, 1975; *Tucker and Bradley*, 2010; *Gabet and Mendoza*, 2012]. Much of the work on particle-based hillslope sediment transport has focused on rockfall hazards [e.g., *Bourrier et al.*, 2012], with few studies exploring longer-term implications for landscape evolution [e.g., *Heckmann and Schwanghart, 2013*]. Although less amenable to landscape evolution modeling over long timescales compared to continuum models, the particle-based approach is more straightforward to connect with field and experimental constraints than nonlocal constitutive laws that require assumptions about the statistics of particle transport.

While a variety of mechanisms drive sediment transport on steep hillslopes, here we focus on the process of dry ravel, the gravity-driven bouncing, rolling, and sliding of particles

commonly observed in steep semi-arid and arid landscapes [*Gabet*, 2003] and in other climates following disturbance (e.g., fire, biotic activity, mass wasting) [*Bennett, 1982*; *Jackson and Roering*, 2009]. In steep landscapes following wildfire, debris flows are in part driven by in-channel bed failure of sediment delivered by dry ravel from adjacent hillslopes [*Wells*, 1987; *Florsheim et al.*, 1991; *Kean et al.*, 2011; *Lamb et al.*, 2011]. In contrast to models that implicitly or explicitly assume transport-limited conditions [*Roering and Gerber*, 2005; *Cannon et al.*, 2010], the magnitude of such debris flows in bedrock landscapes is ultimately limited by hillslope sediment supply and the dynamics of sediment storage, release, and transport associated with vegetation burning on slopes steeper than the angle of repose [*Lamb et al., 2011*; *DiBiase and Lamb*, 2013]. Characterizing the degree of hillslope-channel coupling in wildfire-prone landscapes by dry ravel is thus a key linkage between hillslope mass-balance models [*Lamb et al.*, 2011] and models for in-channel debris flow initiation and transport [*Takahashi*, 1978; *Kean et al.*, 2013; *Prancevic et al.*, 2014].

Here we combine a particle-based model of dry ravel and hillslope-scale experiments to demonstrate how slope, grain size, and surface roughness control the spatial pattern of steep hillslope sediment transport. We frame our analysis using a modified sliding-block analog [*Kirkby and Statham*, 1975; *Gabet and Mendoza*, 2012] to describe the suite of transport modes encompassed by dry ravel (i.e., bouncing, rolling, and sliding). Our hillslope dry ravel experiments provide new data to constrain the frictional properties of dry ravel transport as a function of particle size and surface micro-roughness, as characterized by centimeter-scale topographic surveying with a terrestrial laser scanner. We use our physical experiments to first inform and calibrate a 1D dry ravel model, and ultimately predict the spatial patterns of deposition and nonlocal transport processes in a new 2D ravel-routing model. Then, we discuss the implications of our field and numerical experiments for grain-

size dependent hillslope sediment transport, hillslope-channel connectivity, post-wildfire debris flow hazards, and landscape evolution.

## 2 Theoretical framework

### 2.1 Particle-based ravel transport model

We model dry ravel using a particle-based approach that extends purely probabilistic treatments [*Tucker and Bradley*, 2010] with a simple sliding block model [*Kirkby and Statham*, 1975; *Gabet and Mendoza*, 2012] in order to track the acceleration and deceleration of particles as they move downslope and explicitly account for variations in slope, grain size, and surface roughness. A particle-based approach, although computationally expensive, enables a straightforward incorporation of complex topography and pathways, and does not require assumptions about the statistics of particle motion that underlie continuum models [e.g., *Foufoula-Georgiou et al.*, 2010].

Following previous work [*Kirkby and Statham*, 1975; *Gabet and Mendoza*, 2012], we treat the processes of particle bouncing, rolling, and sliding with a modified Coulomb friction law:

$$A = g(\sin\theta - \tan\varphi\cos\theta) - \kappa|V|^a, \qquad (1)$$

where $A$ is the downslope acceleration of the particle, $V$ is the particle velocity, $g$ is gravitational acceleration, $\theta$ is the local topographic slope, $\varphi$ is an effective (dynamic) friction angle between the particle and the hillslope, $\kappa$ is a dimensional coefficient that controls the strength of a velocity-dependent shock term [*Quartier et al.*, 2000; *Gabet and Mendoza*, 2012], and $a$ is an exponent that is typically 1 or 2 [*Batrouni et al.*, 1996; *Quartier et al.*, 2000]. The magnitude of the shock term ($\kappa|V|^a$) reflects momentum loss due to particle collisions with the hillslope and depends on the contact mechanics. For example, momentum loss may scale with particle velocity ($a$ =1) or particle kinetic energy ($a$ =2). In general, as a

particle moves downhill, it accelerates on local slopes steeper than the effective friction angle $\varphi$ and decelerates on local slopes less than $\varphi$ (or at high velocities due to the shock term).

To implement Equation (1) numerically, a particle is sent downslope with an initial velocity $V_0$ and travels via a number of "hops" until it comes to rest ($V \leq 0$). Consequently, we treat the interaction between the particle and topography as purely due to bouncing; momentum losses due to sliding and rolling are incorporated at each "hop" through the frictional term in Equation (1). Particle velocity, $V$, is updated for each time step $i$ of length $\Delta t$ according to:

$$V_{i+1} = V_i + A_i \Delta t. \tag{2}$$

Equation (2) requires the explicit setting of a time step $\Delta t$, which along with velocity $V$ controls the distance traveled by the particle in each step. Additionally, a length scale $\Delta x$ emerges when choosing the surface slope $\theta$, which controls the scale of topographic variability that influences the patterns of accelerations and decelerations sampled by a particle moving downslope (see Section 2.2). Below this scale, hillslope microtopography is incorporated through the effective dynamic friction slope, $\tan \varphi$, which is thought to depend on the ratio of a characteristic surface roughness height, $k$, and particle diameter, $D$ [*Kirkby and Statham*, 1975; *Gabet and Mendoza*, 2012], similar to (static) particle friction angles in gravel-bedded rivers [*Miller and Byrne*, 1966; *Buffington et al.*, 1992].

We follow *Gabet and Mendoza* [2012] and treat the effective friction slope, $\tan \varphi$, as a stochastic variable that represents the interaction of the grain with randomly distributed topographic roughness elements:

$$\tan \varphi = \mathrm{pdf}(\tan \mu) = \frac{1}{\tan \overline{\mu}} \exp\left(-\frac{\tan \mu}{\tan \overline{\mu}}\right), \tag{3}$$

where pdf($\tan \mu$) indicates an exponential probability distribution of the random variable $\tan \mu$, and $\tan \overline{\mu}$ is the mean effective friction slope. We use an exponential distribution for simplicity and note that the first-order characteristics of most surface grain size and roughness height distributions can be adequately described by such a treatment (Section 4.1). In some cases, stochastic distributions that incorporate additional parameters (e.g., Weibull or lognormal distributions) may be more appropriate.

The time step size, $\Delta t$, which reflects an average hop time, influences the sampling of the distribution of effective friction slopes in Equation (3), and thus controls the degree of particle interaction with the hillslope. Depending on the magnitude of $\Delta t$ relative to the ratio of slope-wise hillslope length, $L_s$, to the mean particle velocity, $V_{mean}$ (averaged over a full transport event), two end-member behaviors emerge. For very small $\Delta t$ ($\Delta t << L_s/V_{mean}$), simulated particle motions become deterministic, and thus require either an increased explicit description of microtopography (decreased $\Delta x$), or a bulk parameterization based on larger grid scales (e.g., continuum slope-dependent transport model). For very large $\Delta t$ ($\Delta t \rightarrow L_s/V_{mean}$), no interaction between the particle and the hillslope is simulated, as the particle traverses the hillslope in a single "hop".

Ideally, the scales $\Delta x$ and $\Delta t$ are linked, such that $\Delta x \sim V_{mean} \Delta t$, where the values $\Delta x$ and $\Delta t$ reflect the observed interaction between the particle and topography. We use a simple scaling argument to estimate hop time *a priori*, treating particle motion as a series of saltation hops with hop height (normal to the surface) the same order as the particle diameter, $D$ [e.g., *Sklar and Dietrich*, 2004]. On a flat plane, the time per hop can be described by time required for a particle to rise and fall a distance $D$ under gravitational acceleration based on conservation of energy:

$$\Delta t \approx 2\sqrt{2D/g}. \qquad (4)$$

As hillslopes steepen, this timescale should increase by a factor of $1/\cos\theta$ to account for the difference between slope-normal hop height and gravitational acceleration. However, complications likely arise for very steep slopes—hop time may increase due to increased mean velocity and larger bounces, or decrease due to increasingly slope-parallel trajectories. Alternatively, $\Delta x$ and $\Delta t$ can be directly measured from experiments, although this is challenging because particle motions often consist of a combination of bouncing, rolling, and sliding.

The magnitude of the shock term coefficient, $\kappa$, as well as the scaling of the shock term with velocity set by the exponent $a$ (i.e., linear or quadratic) must be determined empirically. Equation (1) indicates that there exists a tradeoff between the magnitude of the shock term, $(\kappa|V|^{a})$, and the frictional term, $(g\tan\varphi\cos\theta)$, in controlling particle deceleration, and thus travel distance. For the limiting case of $\kappa = 0$, particles will continue to accelerate on slopes steeper than the friction slope, and quickly achieve unrealistic velocities. For $\tan\varphi = 0$, no disentrainment is predicted and particles will travel at a constant velocity. The details of partitioning between frictional resistance and momentum losses from shocks are poorly constrained for natural systems, and for the scope of this study the inclusion of the shock term serves mainly to limit the maximum particle velocity. For simplicity we assume $a = 1$ and hold $\kappa$ constant, and thus choose to focus on the controls of the effective friction slope, $\tan\varphi$, in controlling particle travel distance.

While our model is simplified and treats an ensemble of processes in bulk, there is good agreement with experiments of scree slope evolution and dry ravel transport [*Kirkby and Statham*, 1975; *Gabet and Mendoza*, 2012]. The particle-based approach is straightforward to expand in two dimensions over complex topography using flow-routing algorithms, and may inform key parameters for 2D nonlocal frameworks [e.g., *Foufoula-Georgiou et al.*, 2010; *Furbish and Roering*, 2013]. Although we focus on the case of a single

particle traveling over a rough surface, the above framework for quantifying frictional and inertial momentum losses is general, and may be applicable to dry granular flows with appropriate calibration. Furthermore, the stochastic model we use [*Kirkby and Statham*, 1975; *Gabet and Mendoza*, 2012] is consistent with continuum soil-transport models based on similar assumptions of Coulomb frictional resistance [*Andrews and Bucknam*, 1987; *Roering et al.*, 1999]. As we show in Section 4.5 below, when $\Delta t$ becomes small ($\Delta t << L_s/V_{mean}$) there is an abrupt transition from local, slope-dependent transport to domain-limited transport above a critical slope, as the effective friction slope, $\tan \varphi$, becomes deterministic.

### 2.2 Scale-dependent characterization of hillslope topography

Central to the treatment of dry ravel transport in natural landscapes is an appropriate scale-dependent treatment of surface roughness and topographic variability. From the above model (Equation 1), two key scales emerge: a micro-scale roughness that accounts for the local interaction between a particle and the surface and a macro-scale topographic variability that influences particle acceleration and deceleration over an entire transport event. Importantly, the micro- and macro- definitions of roughness and topographic variability require different methods of characterization appropriate to their influence on dry ravel transport.

At the micro-scale (length scales $< \Delta x$), the interaction between a particle and a rough surface is typically quantified by the size distribution of relative roughness heights, or deviations in elevation from a mean topography normalized by particle diameter, $D$. Roughness heights are either estimated from grain size distributions of surface sediment [e.g., *Miller and Byrne*, 1966] or measured directly using sub-grain-scale microtopography acquired from laser scans or structure-from-motion photogrammetry [e.g., *Brasington et al.*, 2012]. Here we used both approaches to characterize hillslope micro-roughness height

distribution (see Section 3.2), which is incorporated into Equation (1) through the (stochastic) effective dynamic friction slope, $\tan\varphi$ (Equation 3).

At the macro-scale (length scales $> \Delta x$), topographic variability controls particle transport through its influence on the sequence of accelerations and decelerations integrated over an entire transport event. Thus, rather than depending on the variation in elevation deviations, macro-topography effects should depend on the variability of the surface slope $\tan\theta$. Importantly, Equation (1) indicates that particle acceleration on slopes steeper than the effective friction slope, even in the absence of the shock term, is less than the corresponding deceleration on slopes similarly shallower than the effective friction slope. Thus, hillslopes characterized by slopes variably steeper and shallower than the friction slope should lead to a net decrease in travel distance relative to uniform slopes. By definition, topographic variability is directly resolved when Equation (1) is applied to natural landscapes. However, in order to test model sensitivity to topographic variability in 1D simulations we define a metric of topographic variability, $\sigma_\theta$, as the standard deviation of surface gradient $\tan\theta$.

## 3 Field experimental methods

### 3.1 Field site and description of experiments

To calibrate the parameters for the particle-based model described above, we performed a series of dry ravel experiments on a steep hillslope near Mount Wilson in the San Gabriel Mountains, CA (Figure 1). Although near the perimeter of the 2009 Station Fire, this region has not burned since 1898 (Fire and Resource Assessment Program, California Department of Forestry and Fire Protection, http://frap.cdf.ca.gov). The studied hillslope is characterized by an unvegetated 30-m long, planar, 38-40° colluvial deposit at the base of a steep (~60°) bedrock cliff. At the bottom of the hillslope is a first-order boulder-bedded channel (Tumble Creek of *Prancevic and Lamb* [2015]). Near our field site, we collected and

painted 194 subangular colluvial particles from 3 size classes for our experiments. With intermediate axis lengths of 2-3 cm, 4-6 cm, and 9-12 cm, the three size classes bracket much of the size range of coarse material mantling the studied slope (Figure 2).

Our ravel experiments consisted of releasing individual particles one at a time from a random orientation at the top of the 30-m-long slope and video recording the particles as they traveled downhill using a compact digital camera (30 frames per second). There was no interaction between individual test particles, and limited secondary avalanching was induced on the hillslope (see Supporting Information Movies S1 and S2). The final position of each particle was then surveyed with a laser rangefinder to an accuracy of ±10 cm.

Video for each particle was analyzed frame-by-frame to determine initial particle velocity, $V_0$, mean particle velocity, $V_{mean}$, and the average hop time, $\Delta t$. To limit the variability in the direction and magnitude of the initial velocity, we packed down a 1.5-m-long smooth dirt ramp at the start and dropped the particles from a constant height of 10 cm. Initial particle velocity, $V_0$, was determined by the time taken to travel the initial 1.5 m ramp. To determine mean particle velocity, $V_{mean}$, we divided the slope-wise particle travel distance, $d$, by the time in motion determined from the video analysis. Determining the average hop time, $\Delta t$, is more challenging because particles travel downslope by a combination of bouncing, rolling, and sliding. For each particle, we divided the time in motion by the number of discrete hops recorded in the video (ignoring rolling and sliding) to obtain a maximum value for $\Delta t$.

Due to an increase in gradient from 38° to 40° at a distance of 14 m down the slope (Figure 1), all particles that survived the first 14 m of travel without stopping traversed the entire slope and were noted as "runners". Thus, we restricted our analysis to the upper 14 m of the studied hillslope, focusing on a 1-m-wide swath that encompasses most of the lateral dispersion of the particles (Figure 3b). We defined a 1D coordinate system that parallels the

slope in the direction of steepest descent to measure downslope travel distance $d$, where $d = 0$ lies at the bottom of the 1.5-m-long ramp where we measured $V_0$. At a 10 m scale, the topography of the experimental hillslope is smooth; in contrast, topography is highly variable over short (< 1 m) wavelengths. To characterize the fine-scale (<1 cm) topography of the hillslope, we performed laser scans with a FARO laser scanner from 2 locations along the hillslope. We aligned and merged the point clouds using the software CloudCompare (http://www.danielgm.net/cc/) and clipped the extent to focus on the 14 m x 1 m area noted above. Total location uncertainty for each point is on the order of 2 mm and the error due to aligning the separate point clouds using only static natural features (e.g., large rocks) is 2.4 cm. Large (>10 cm) data gaps cover approximately 5% of the area due to shadows behind protruding rocks (Figure 3a). To reduce bias from increased data density in areas of overlap, the merged point cloud was randomly sub-sampled to a minimum (3D) spacing of 30 mm, achieving near-uniform point density (95% coverage) and a total of $1.4 \times 10^4$ points. Our metrics of surface micro-roughness are insensitive to point spacing ranging from 5 to 100 mm (see Supporting Information Figure S1), and thus we use a sampling interval of 30 mm to ensure uniform point density when quantifying spatial variations in roughness.

We calculated the surface micro-roughness of our hillslope using two methods. First, in the field we performed a Wolman-style point count [*Wolman*, 1954] of the intermediate axis of 112 surface grains measured following a grid with ~0.3 m point spacing in the upper 6 m of the studied hillslope. The distribution of grain sizes serves as a crude approximation of the distribution of roughness heights, but allows comparison with prior, grain-size-based approaches [e.g., *Kirkby and Statham*, 1975]. Second, we used the hillslope microtopography to calculate $\sigma_z$, the standard deviation of roughness height, along a regularized grid of detrended elevation. Because our surveyed hillslope is nearly planar, the magnitude of $\sigma_z$ is relatively insensitive to the method used to detrend topography (Supporting Information

Figure S2), and we present results from roughness heights determined as the distance of each point to a plane fit through the 14 m x 1 m study region. The magnitude of $\sigma_z$ also depends on the scale of analysis—$\sigma_z$ is expected to increase as a power law with observation scale at sub-grain length scales and become constant at larger scales [e.g., *Nikora et al.*, 1998]. We calculated $\sigma_z$ along a 1 m x 1 m grid based on the characteristic size of the largest particles (~30 cm) and analysis that suggests a break in scaling at ~0.75 m (Supporting Information Figure S1), consistent with the transition scale between micro and macro-topography defined below as $\Delta x = 1$ m.

## 4 Results of field experiments and 1D uniform slope model

### 4.1 Hillslope micro-topography and roughness characterization results

The full range of roughness heights from the point count and microtopography-based methods are shown in Figure 2. The intermediate axis diameter of surface grains ranges from 0.3 cm to 30 cm, with a median ($D_{50}$) of 3 cm. The three size classes used for our experiments (2-3 cm, 4-6 cm, and 9-12 cm) correspond roughly to $D_{40}$, $D_{75}$, and $D_{90}$ of the surface grain size distribution. Estimates of surface roughness height based on the standard deviation of detrended elevation are of similar magnitude as the surface grain size distribution, and we show in Figure 2 distribution of both the detrended roughness heights and the value of $\sigma_z$ for each 1 m x 1 m grid cell. We used $\sigma_z$ to calculate the spatial patterns of relative roughness (roughness height normalized by grain diameter) for our three experiments (Figure 3c) and note that the variability in relative roughness of the hillslope is generally less than the variability between different grain size experiments (Figure 3c). For simplicity we assumed that there are no systematic spatial variations in $\tan \overline{\mu}$ over length scales greater than 1 m when simulating our field experiments (Section 4.3).

### 4.2 Field and experimental results

We find that particle (slope-wise) travel distance, *d*, varies systematically with the ratio of particle diameter to roughness height, as in previous experiments [*Kirkby and Statham*, 1975; *Statham*, 1976]. Additionally, particle transport is characterized by a domain-limited, thin-tailed distribution of travel distances. For the size class 2-3 cm, 53 of 58 particles stopped within the first 14 m, and of these, many stopped within 4 m (Figure 4). For the size class 4-6 cm, particles were also concentrated in the first 4 m, although with a larger fraction traveling the entire length of the hillslope (33% "runners"). For the size class 9-12 cm, 67% of the particles traversed the entire hillslope. Thus, in addition to a systematic increase in travel distance for particles that remained on the study hillslope, there was a clear increase in the number of runners—particles deposited directly to the channel at the foot of the hillslope—with increasing particle size class. Initial velocity, $V_0$, varies minimally within each set of experimental runs, but increases weakly with grain size between the three size classes (Table 1, Supporting Information Table S1). Mean and maximum values of $V_{mean}$ (mean particle velocity over a single transport event) range from 1.5-3.2 m/s and 3.0-5.1 m/s, respectively, with higher velocities corresponding to larger grain size classes (Table 1, Supporting Information Table S1). Most particles moved downslope through a combination of bouncing, rolling, and sliding, with bouncing being the dominant mode of transport. Measured hop time, $\Delta t$, which ranges from 0.2-0.8 s, shows no systematic variation with particle size and lies in the range predicted by Equation (4) (Supporting Information Table S1).

### 4.3 Comparison of field experiments to numerical model

We aimed to simulate our three hillslope experiments using a 1D particle-based model in order to calibrate the mean effective friction slope, $\tan \bar{\mu}$, and the shock term coefficient, $\kappa$, for each of three particle size classes (*D* = 2-3 cm, 4-6 cm, and 9-12 cm). We characterized

the macro-topography of the experimental hillslope as a 15 m long, 38° uniform slope ($\tan \theta$ = 0.79). For each of 10,000 simulations per particle size class, an individual particle was given an initial velocity, $V_0$, at the top of the slope and tracked as it accelerated or decelerated according to Equations (1) and (2) until coming to rest ($V \leq 0$). We varied $V_0$ as a function of particle diameter, based on results from field experiments (Table 1). Counting the number of discrete bounces provides an average hop time of 0.3 s, while using Equation (4) results in hop time estimates that range from 0.2-0.4 s, depending on particle diameter. As there is no clear trend between particle size and hop time seen in the field experiments, we used a constant value of $\Delta t = 0.3$ s for all runs.

After choosing a value for $\Delta t$, we tuned the shock term coefficient $\kappa$ to match modeled and observed maximum values of mean particle velocity, $V_{\text{mean}}$ (i.e., highest mean velocity for a single transport event). The best-fit $\kappa$ decreases with increasing grain size, from 0.8 to 1.6 s$^{-1}$ (Supporting Information Figure S4). However, because there is a tradeoff between $\kappa$ and $\tan \bar{\mu}$ for a given transport distance, we hold $\kappa$ constant for all runs and focus on the variation of the mean effective friction slope, $\tan \bar{\mu}$, with changing grain size. We found that a value of $\kappa = 1.4$ s$^{-1}$ results in similar mean and maximum event-averaged particle velocities for the intermediate size class (4-6 cm particles), but over- and underestimates velocities for the 2-3 cm and 9-12 cm particles by 10-30% (Table 1). Next, we varied the mean effective friction slope, $\tan \bar{\mu}$, such that the mean travel distance equaled that measured in the field ("runners" were counted as $d = 14$ m, for consistency with the limit of our field measurements). We find that the magnitude of the mean effective friction slope, $\tan \bar{\mu}$, decreases with increasing particle diameter and ranges from 0.37 to 0.56 m/m (Figure 4). For all cases, the combination of Equations (1), (2), and (3) captures the first-order variability in transport behavior, and we move forward using these values to constrain our particle-based model.

### 4.4 Nondimensional framework for evaluating local versus nonlocal transport

To generalize our analysis to an arbitrary 1D uniform slope, we evaluated how the parameters $\tan\bar{\mu}$, $V_0$, $\Delta t$, and $\kappa$ in Equations (1), (2), and (3) influence the relationship between mean travel distance and hillslope gradient. We normalize mean travel distance, $\bar{d}$, by hillslope length, $L_s$, resulting in a dimensionless parameter $d^* = \bar{d}/L_s$ that scales with hillslope sediment flux. The normalized mean travel distance, $d^*$, can also be thought of as a ratio of advection length scale to landform length scale or domain size and thus determines the degree to which particles morphodynamically interact with the hillslope [*Ganti et al.*, 2014]. We scale mean hillslope gradient, $\tan\bar{\theta}$, by the mean effective friction gradient, $\tan\bar{\mu}$, to define a normalized hillslope gradient, $S^* = \tan\bar{\theta} / \tan\bar{\mu}$. For all model runs, we fixed hillslope length, $L_s$, to 100 m, based on regional analysis of lidar-derived topography in the San Gabriel Mountains [*DiBiase et al.*, 2012]. Each run cycled through 25 hillslope gradients, with $S^*$ ranging from 0.01 to 5, and tracked 10,000 particles launched from the top of each slope with initial downslope velocity, $V_0$.

As a baseline run we used values from Section 4.3 to estimate parameters for the simple case of uniform particle size and surface micro-roughness. We use $V_0 = 2$ m/s, $\Delta t = 0.3$ s, and $\kappa = 1.4$ s$^{-1}$, as in our field experiments, and assume $\tan\bar{\mu} = 0.5$ for the case where particle size and surface micro-roughness are of similar magnitude. Due to the stochastic treatment of the mean effective friction slope (Equation 3), there is a broad transition from short mean travel distance at the lowest slopes (limit of $d^* = V_0\Delta t/L_s$ for $S^* = 0$) to all particles exiting the hillslope at the steepest slopes ($d^* = 1$ for $S^* > 4$) (Figure 5). Notably, the transition to $d^* = 1$ does not occur until slopes that are significantly steeper than the friction slope.

We use the $d^*$ framework of travel distance normalized by hillslope length in order to characterize the transition from local to nonlocal transport that occurs as the normalized

slope, $S^*$, increases. In a strict sense, the condition of nonlocal transport requires a heavy-tailed distribution of travel distances such that there is no choice of observation scale (i.e., representative elementary volume) sufficient to characterize fluxes using local quantities. However, because field-measured and model-derived particle travel distance distributions are not heavy-tailed, the definition of local versus nonlocal transport depends on the scale of observation. Moreover, sediment transport distances are always bound to have a physical upper limit, which will define the scales over which the distribution of the sediment transport distances is defined. For the case of hillslope sediment transport, the largest scale of observation is set by the hillslope length. Thus, we use the term "purely nonlocal" to describe events where particles traverse nearly the entire hillslope ($d^* > 0.95$) and transport distance is domain-limited. We use the term "local" transport to describe events that have transport distances that are short relative to the hillslope length ($d^* < 0.05$), and thus where local slope and roughness are sufficient to determine sediment flux. For intermediate transport behavior ($0.05 > d^* > 0.95$), we use the term "transitional". For typical combinations of hillslope lengths (10 m - 1 km) and scales of landscape analysis (1 - 100 m), both purely nonlocal and transitional transport behavior are sensitive to particle path history and thus flux cannot be described with local variables.

### 4.5 Sensitivity analysis for 1D uniform slope model

We varied $\tan \bar{\mu}$, $V_0$, $\Delta t$, and $\kappa$ systematically to evaluate their controls on hillslope sediment flux as expressed by the relationship between $d^*$ and $S^*$ (Table 2). Changing the mean effective friction slope, $\tan \bar{\mu}$, weakly influences the relationship between $d^*$ and $S^*$, as most of the variation is captured by the normalization of hillslope gradient encapsulated by $S^*$ (Figure 6a). Likewise, variation in initial velocity up to $V_0 = 4$ m/s has little influence on the resulting mean travel distance (Figure 6b), suggesting that the influence of $V_0$ is minimal for $V_0 \Delta t / L_s < 0.01$. In contrast, the average hop time, $\Delta t$, directly influences the sharpness of the

transition from local to nonlocal transport (Figure 6c), by controlling the number of values

sampled from the stochastic distribution of friction slope, as described in Section 2.1. For the

range of $\Delta t$ shown, the primary sensitivity in the $d^*$-$S^*$ relationship is the slope required to

achieve purely nonlocal behavior ($d^* \sim 1$). The sample size used for Equation (3) controls the

likelihood of a particle stopping on a slope significantly steeper than the friction slope.

Particle travel distance for $S^* < 1.5$ is less affected by the magnitude of $\Delta t$. Note that the case

of $\Delta t = 0.1$ s is similar to the model and experimental data used by *Gabet and Mendoza*

[2012], although we find that their data are better fit with $\kappa = 1.4$ than the reported value of $\kappa$

$= 0.0175$ (Supporting Information Figure S3). The magnitude of the shock term coefficient,

$\kappa$, also influences mean particle travel distance by clipping the upper limit of particle velocity

(Figure 6d). While $\kappa$ can be tuned to match modeled to observed velocities (Supporting

Information Figure S4), determining the velocity dependence (i.e., linear or quadratic) of the

shock term in Equation (1) is more challenging and requires experiments where initial

velocity varies in a controlled manner to isolate this effect, which we do not tackle here. In

addition, $\kappa$ likely depends on the substrate and particle properties, with higher values (i.e.,

more energy losses) for soil than for bare rock.

**5 Model results for more complex terrain**

*5.1 Incorporation of macro-scale topographic variability in 1D*

As discussed in Section 2.2, macro-scale topographic variability refers to changes in

slope, $\tan \theta$, that occur over distances greater than $\Delta x$ and thus influences the acceleration

and deceleration particles according to Equation (1). To quantify the importance of

topographic variability on particle transport distance, we analyzed hillslope elevation profiles

in the San Gabriel Mountains and then incorporated this effect into our 1D particle transport

model.

Using 1-m-resolution gridded lidar topography from the San Gabriel Mountains, we extracted 28 1D elevation profiles spanning a range of hillslope morphology (Supporting Information Data Set S3). We assume a break between macro- and micro-topography at $\Delta x = 1$ m. Although limited by the resolution of the airborne lidar topography, a scale of $\Delta x = 1$ m is similar to the scaling break observed from analysis of microtopography of our study site (Supporting Information Figure S1), is consistent with hop lengths observed in our experiments, and is in agreement with estimates based on $\Delta t$ and $V_{mean}$ measured from the field experiments ($V_{mean}\Delta t = 0.4 - 1.0$ m). From the 28 elevation profiles, each chosen to have a fixed slope length of $L_s =100$ m, we calculated local hillslope gradient at a scale of $\Delta x = 1$ m along the entire profile and calculated the topographic variability, $\sigma_\theta$, as the standard deviation of local hillslope gradient, $\tan\theta$ (Figure 7). We determined $S^*$ using the average hillslope gradient, $\tan\overline{\theta}$, for each hillslope and assuming $\tan\bar{\mu} = 0.5$ for consistency with the above 1D simulations (Section 4.4). Hillslopes with mean gradient less than 0.7 ($S^* < 1.5$) tend to be mantled with soil [*DiBiase et al.*, 2012] and correspondingly smooth (blue profile, Figure 7). For steeper hillslopes ($S^* > 1.5$), $\sigma_\theta$ increases systematically with mean gradient as hillslopes become rockier (Figure 8).

To incorporate macro-scale topographic variability into our 1D model from Section 4.4, we used the relationship between slope and slope variability from the San Gabriel Mountains (Figure 8) to define a simple piecewise linear relationship between $S^*$ and $\sigma_\theta$, where $\sigma_\theta = 0.1$ for $S^* < 1.5$ and $\sigma_\theta = 0.39 S^* - 0.49$ for $S^* > 1.5$. We generated a randomized topography for each model iteration, built from a Gaussian distribution of $\tan\theta$ with a mean of $\tan\overline{\theta}$ and standard deviation $\sigma_\theta$. For a single value of $S^*$, we simulated 10,000 particles, each traversing a different topographic profile. Values for $\tan\bar{\mu}$, $V_0$, $\Delta t$, and $\kappa$ were set to the baseline case described in Section 4.4 (Table 2).

Our results show that particle transport distance decreases with increasing topographic variability, due to the asymmetry in accelerations predicted by Equation (1) for slopes steeper and less steep than the friction slope, as described in Section 2.2. For low to moderate slopes ($S^* < 1.5$), topographic variability is minimal (Figure 8) and thus normalized mean transport distance, $d^*$, is similar to the baseline case ($\sigma_\theta = 0$; Figure 9). As slopes steepen beyond $S^* = 1.5$, there is increasing divergence in model predictions for hillslopes incorporating topographic variability due to the positive relationship between $S^*$ and $\sigma_\theta$, and normalized mean transport distance decreases significantly for steep slopes (Figure 9). For the steepest slopes ($S^* > 3$), our model predicts a 60%-75% decrease in transport distance (and thus sediment flux) when accounting for the influence of topographic variability.

The above analysis highlights both the importance of accounting for multiple scales of surface roughness and topographic variability and the challenges associated with choosing a characteristic length scale to delineate micro- versus macro-topography. The increasing availability of high-resolution topography from lidar and structure-from-motion photogrammetry means that surface topography and roughness can be readily characterized at multiple scales ($10^{-3}$ - $10^{1}$ m) and across whole hillslopes [e.g., *McKean and Roering*, 2004; *Pollyea and Fairley*, 2011; *Smith*, 2014], allowing the choice of measurement scale to be set by the process and grain size [*Roering et al.*, 2010], or alternatively through multi-scale analysis of topographic roughness [e.g., *Nikora et al.*, 1998]. However, detailed topographic surveys of grain-scale roughness (e.g., Figure 3a) are often limited in spatial extent due to data collection or processing challenges. Thus, characterizing the spatial heterogeneity in micro-topography and effective dynamic friction slope requires either a) parameterizing roughness at scales smaller than the grid size from macro-topography (e.g., airborne lidar data) and surface cover mapping (e.g., soil, rock, vegetation type) or b) parameterizing sub-grid-scale sediment flux models [e.g., *Ganti et al.*, 2012].

### 5.2 2D ravel routing model

The particle-based approach to hillslope dry ravel transport described above is straightforward to expand in two dimensions to the landscape scale through the use of a flow-routing algorithm that routes 1D particle paths through a digital elevation model. By simulating the paths of multiple particles released from each source location, it is possible to generate statistical descriptions of particle transport across the entire landscape and explicitly track spatial patterns of hillslope deposition. In this manner, it is possible to account for not only spatial changes associated with convergent or divergent topography (e.g., valleys and ridges), but also more complicated patterns of slope and surface roughness: rough bedrock hillsides, smooth soil-mantled hillslopes, and temporary sediment sinks such as terrace flats or swales. Variations in both the amount and style (i.e., local or nonlocal) of hillslope sediment transport and deposition across the landscape are important for predicting short-term hazards (e.g., sediment loading of debris flow channels following wildfire) and for quantifying the nature of hillslope-channel coupling necessary for modeling the longer-term evolution of steep landscapes.

For the 2D ravel routing model, we applied Equations (1), (2), and (3) to a 2.5 km$^2$ region encompassing our study hillslope in the San Gabriel Mountains, California (Figure 10a; Supporting Information). We used a 1-m-resolution, lidar-derived bare-earth digital elevation model as our macro-topography and for simplicity held this fixed with time (i.e., no evolving of topography with erosion and deposition). The expansion to 2D was achieved through a series of 1D simulations routed down flow paths governed by topography. Each particle simulation down a flow path is similar to the 1D model described in Section 5.1, except that actual, rather than statistical, topography is used.

At each grid cell, a particle is released in the direction of steepest descent with initial velocity, $V_0$, and then routed using a probabilistic flow routing algorithm linearly weighted by

the downslope gradient to adjacent cells [*Dorren et al.*, 2004]. For a given cell, the downstream gradient in each of 8 directions is calculated and then used to weight the choice of flow direction. Thus, over the course of multiple particle simulations, flow is focused in convergent swales and gullies, where there is typically a single path of steepest descent, and allowed to spread on planar or divergent hillslopes, where there may be multiple paths with similar slope. For simplicity, we do not explicitly model momentum losses associated with changes in direction [*Howard et al.*, 1994], or weight the choice of flow path by particle momentum. In general, particle paths on hillslopes are straight, rather than tortuous, and we assume that these directional effects are encapsulated within the field-calibrated friction slopes.

At each grid cell, we kept track of three key model outputs: first, we recorded the slope distance traveled, *d,* for each particle that started from each cell in order to characterize the spatial pattern of sediment sources that generate local versus nonlocal transport; second, we recorded the slope distance traveled for each particle that comes to rest at each cell in order to characterize the locality or nonlocality of sediment sinks in the landscape; and third, we recorded the total number or particles deposited at each cell. All parameters for this scenario were fixed to the baseline case described in Section 4.4 (Table 2).

Figure 10 shows the results from a single simulation where 20 particles were initiated from each grid cell, for a total of $5 \times 10^6$ particles. In general, most deposition occurs in the convergent parts of the landscape, with thicker deposits in valley bottoms below steeper hillslopes and more diffuse deposition on less steep hillslopes (Figure 10b).

To better visualize the spatial patterns of local and nonlocal hillslope sediment transport, we mapped the distribution of average particle travel distance for ravel sources (Figure 10c) and for ravel sinks (Figure 10d). The map of mean source travel distance (Figure 10c) indicates the average slope distance traveled for particles that were initiated from each

grid cell. Because the mean hillslope length, $L_s$, is on the order of 100 m [*DiBiase et al.*, 2012], we consider transitional or nonlocal transport to be defined as particles having travel distance $d > 5$ m ($d^* > 0.05$; Figure 5). Likewise, the map of mean sink travel distance (Figure 10d) highlights deposits consisting of material that is far-traveled. Figures 10c and 10d emphasize regions of the landscape where the assumptions of local transport are suspect and the spatial arrangement of steep slopes must be accounted for (i.e., $d^* > 0.05$). Our particle-based model also allows for straightforward extraction of statistical distributions of travel distance, velocity, and disentrainment rate that are key for the comparison to and development of continuum nonlocal formulations [e.g., *Furbish and Roering*, 2013].

The example shown is simplified, in that we assume that ravel production, initial velocity, $V_0$, and mean effective friction slope, $\tan\overline{\mu}$, are uniform across the landscape, and topography does not evolve. For example, it is likely that the source of ravel depends on slope, soil and vegetation cover, and spatial and temporal patterns in wildfire burn intensity [*Lamb et al.*, 2011; 2013; *DiBiase and Lamb*, 2013]. Additionally, at a minimum, surface micro-roughness depends on surface cover (soil vs. bedrock), grain size, and vegetation patterns. Even so, the patterns shown in Figure 10 broadly match our qualitative field observations of colluvial deposit thickness and the above factors can be readily incorporated into this framework in future studies.

## 6 Discussion

### 6.1 Grain size and roughness controls on hillslope sediment transport and storage

Our experimental results highlight the sensitivity of hillslope sediment transport to grain size and surface roughness (Figure 4). Comparison of our data with prior field and laboratory experiments [*Kirkby and Statham*, 1975; *Statham*, 1976; *Gabet and Mendoza*, 2012] indicates broadly similar scaling between surface roughness normalized by grain size

($k/D$, where $k$ is a characteristic roughness height) and the mean effective dynamic friction slope, $\tan \bar{\mu}$ (Figure 11). For uniform grain size ($k/D = 1$), $\tan \bar{\mu}$ is approximately 0.5 ($\bar{\mu} = 27°$). However, for the typical range of grain sizes present on our experimental hillslope ($k/D = 0.1 - 3$), $\tan \bar{\mu}$ ranges from 0.25 to >1.0 ($\bar{\mu} = 14°$ to >45°), highlighting a wide range of grain-size dependent disentrainment rates once particles are mobilized. Additionally, dynamic friction slopes are considerably less than laboratory or field measured static friction slopes, but also increase with increasing relative roughness (Figure 11) [*Kirkby and Statham*, 1975; *Statham*, 1976]. Thus, the increased stresses required to initiate motion of large particles may be offset by lowered relative roughness compared to smaller grains, similar to what has been found in fluvial sediment transport [e.g., *Wiberg and Smith*, 1987; *Kirchner et al.*, 1990], emphasizing the importance of grain-size-dependent transport behavior for controlling landscape-scale patterns of grain size and roughness.

Because the mean effective dynamic friction slope, $\tan \bar{\mu}$, is sensitive to grain size for a given hillslope, whether particles exhibit local or nonlocal transport is also a function of grain size. On soil mantled hillslopes, an assumption of uniform grain size and surface roughness may be warranted and thus the assumption of a single critical friction slope appropriate [e.g., *Roering et al.*, 1999]. In contrast, sediment transport on bedrock hillslopes is likely to involve a wider range of grain sizes and spatial variability in both micro- and macro-topography (e.g., Figure 4, Figure 8). As indicated by our 2D models, topographic variability imparts a strong spatial heterogeneity of sediment stability and storage on hillslopes, even with an assumption of uniform mean dynamic friction slope (Figure 10). Thus, the transition zone between local and nonlocal transport (Figure 5) is likely to dominate the extent of steep, rocky landscapes, with the implication that sediment transport cannot adequately be captured by a single friction slope [*Gabet and Mendoza*, 2012]. Rather, as shown by our field experiments, fine sediment will tend to be sequestered by roughness

elements on hillslopes, while coarse debris is more prone to bypass hillslope storage zones and be delivered to the channel network directly.

An important consequence of accounting for topographic and vegetation roughness on steep hillslopes is the resulting increase in sediment stability on steep hillslopes that influences soil residence time and hillslope weathering in steep landscapes [e.g., *Dixon et al.*, 2012; *Heimsath et al.*, 2012; *West*, 2012; *Larsen et al.*, 2014]. Notably, most landscape evolution models predict zero residence time for sediment on hillslopes steeper than a uniform friction slope, where soil transport greatly exceeds local rates of soil production [*Dietrich et al.*, 2003; *Tucker and Hancock*, 2010]. In contrast, our model predicts significant residence times in steep, rocky landscapes due to the enhanced trapping of finer grain sizes. Additionally, due to macro-topographic variability, even very steep slopes ($3 < S^* < 5$) fail to exhibit purely nonlocal, domain-limited transport ($d^* \sim 0.2$ - $0.3$; dashed line in Figure 9), in agreement with observations of patchy soils retained in steep landscapes [*Heimsath et al.*, 2012; *DiBiase et al.*, 2012].

### 6.2 Implications for landscape connectivity

The combination of grain-size dependent sediment transport and spatiotemporal variations in surface roughness and macro-topography implies a richer diversity of landscape behavior not captured by continuum models of hillslope sediment transport that assume a uniform friction slope for hillslope material. For example, even a steep (38° - 40°) colluvial deposit such as in our study hillslope can serve as both a temporary sink for sediment sourced from steeper slopes uphill and as a sediment source for the downstream channel network. Temporary (dry) storage areas can allow accumulation to fuel larger mass failures in "wet" debris flow initiation zones, either on hillslopes [e.g., *Reneau and Dietrich*, 1987] or in channels [e.g., *Prancevic et al.*, 2014]. In steep landscapes, temporary sediment sinks in the transitional slope zone may be the largest generator of landslides and hazards due to temporal

variations in stability and because such slopes (~30° - 45°) comprise the bulk of the landscape [*Lamb et al.*, 2011; *DiBiase et al.*, 2012]. In these transitional zones (Figure 5), we hypothesize that slopes are low enough to accumulate material, but steep enough to readily fail. Thus it is necessary not simply to characterize the net mass flux, but also the retention timescales that lead to stochastic sediment delivery into channel networks [*Benda and Dunne*, 1997].

Our results also show that larger grains have lower effective dynamic friction slopes (Figure 4), which influences the timing and pattern of sediment delivery from hillslopes to channels. In soil-mantled landscapes, the grain size distribution of material delivered to the channel network is likely well-mixed and a function of mean residence time and degree of chemical alteration [*Attal et al.*, 2015]. However, in steep rocky landscapes, our model predicts that sediment delivered to the channels by dry ravel will be enriched in coarser grains, a result corroborated by our hillslope experiment showing an increase in the number of particles traversing the entire hillslope with increasing grain size. The downslope coarsening of bedrock hillslope sediment transport, long noted in studies of rockfall and talus cone evolution [*Rapp*, 1960; *Kirkby and Statham*, 1975], leads to a convergence of coarse material in headwater channels that may help explain the observed pattern of downstream coarsening at small drainage areas in fluvial systems [e.g., *Brummer and Montgomery*, 2003].

The stochastic, grain-size dependent transport on hillslopes also has implications for quantifying landscape connectivity and the coupling between hillslopes and channels [*Heckmann and Schwanghart*, 2013; *Bennett et al.*, 2014]. By using a particle-based approach in 2D (Figure 10), it is possible to explicitly treat the delivery of grain size distributions from bedrock hillslopes to channels that is important for setting channel slope [*Hack*, 1957], controlling bedrock river incision [*Sklar and Dietrich*, 2006], and influencing the interpretation of detrital geochronology sampling techniques [*Riebe et al.*, 2015]. By

highlighting potential storage zones in steep landscapes (Figure 10b, 10d), our 2D ravel routing model can aid in targeting sites for quantifying grain-size dependent timescales of sediment storage in mountainous landscapes.

### 6.3 Implications for post-wildfire debris flow hazards

A key application of our model lies in the characterization of spatial patterns of post-wildfire debris flow hazards common in the steep, semi-arid landscapes of southern California and elsewhere [*Cannon et al.*, 2010]. In soil-mantled landscapes, post-wildfire debris flows are fueled by discrete shallow landslides or distributed rilling on hillslopes following storms [e.g., *Wells*, 1987; *Gabet*, 2003]. In contrast, post-wildfire debris flows in bedrock landscapes are thought to initiate through in-channel bed failure of sediment delivered from hillslopes by dry ravel following the burning of vegetation dams [*Florsheim et al.*, 1991; *Lamb et al.*, 2011; *Prancevic and Lamb*, 2014]. In the San Gabriel Mountains, *DiBiase and Lamb* [2013] showed that the 10- to 30-fold increase in sediment flux recorded in debris retention basins following wildfire [*Lavé and Burbank*, 2004; *Lamb et al.*, 2011] could be explained by the transient storage and release of sediment on hillslopes ranging from 30° - 45°, and quantified the volume and spatial distribution of temporarily stable hillslope sediment sources. However, the coupling of post-wildfire hillslope and channel processes in steep landscapes has been hampered by the ability to adequately characterize the efficiency of hillslope sediment delivery to channels and the spatial patterns of channel loading by dry ravel.

Our 2D ravel-routing model provides a framework to link hillslope storage models [*DiBiase and Lamb*, 2013; *Lamb et al.*, 2013] with sediment transport in channels [*Kean et al.*, 2011; *Kean et al.*, 2013; *Prancevic et al.*, 2014] to better inform predictions of post-wildfire sedimentation hazards. In the simplest scenario, our model results (Figure 10b) indicate that dry ravel is preferentially stored in headwater valley floors adjacent to steep,

rocky hillslopes—areas also subject to enhanced runoff during storms. Our results are consistent with observations that steep channels are temporary sinks for hillslope sediment prior to evacuation by debris flows and can provide insight to the spatial patterns of debris flow hazards due to enhanced hillslope-channel coupling in areas experiencing nonlocal hillslope sediment transport. Because the valleys characterized by the highest amount of ravel deposition are also subject to the highest amount of non-locally-derived sediment (Figure 10), accurate patterns of dry ravel accumulation, especially incorporating grain-size, are unlikely to emerge from existing local hillslope sediment transport models.

More sophisticated models based on our 2D ravel-routing model may also add insight to the contrast between background (unburned) and post-wildfire channel bed state through the inclusion of spatiotemporal variations in surface micro-roughness. In unburned conditions, vegetation adds roughness to hillslopes that preferentially captures fine sediment, with coarse sediment that bypasses hillslope storage zones contributing to a thin alluvial sediment cover in bedrock channels [*DiBiase and Whipple*, 2011]. Following wildfire, the loss of vegetation on hillslopes lowers hillslope surface roughness and enables efficient transport of fine material to channels [*Meyers and Wells*, 1997], which is readily mobilized through in-channel bed failure as debris flows [*Prancevic et al.*, 2014]. Thus, between fires, the temporal variation of surface micro-roughness and spatial patterns of dry ravel transport determine the fraction of sediment production from bedrock that is captured behind vegetation dams, and directly influences predictions of the degree to which bedrock hillslopes will respond to wildfire [*Lamb et al.*, 2011]. With increasing coverage of high-resolution topographic data, these variations in vegetation growth are increasingly likely to be captured through comparison of pre- and post-event topographic-derived vegetation metrics. Additionally, observations and measurements of post-wildfire, but pre-rainfall, dry ravel deposits could be used to help validate or calibrate the 2D ravel routing model and lead to

channel-specific hazard predictions prior to the winter storms that typically trigger the most destructive debris flows.

### *6.4 Implications for landscape evolution*

Our model provides a framework for characterizing hillslope sediment transport in steep landscapes containing a patchwork of soil and rock [*DiBiase et al.*, 2012], and highlights the importance of quantifying the controls on soil production from bedrock that dictate the morphodynamics of steep landscapes. Further work is needed to characterize the frequency and magnitude of disturbances that drive the initial motion of sediment on steep hillslopes and to assess the degree to which particle interactions and mass movement influence the efficiency of sediment transport by dry ravel. Ultimately, in order to reach an equilibrium form, bedrock hillslopes must be tied to baselevel fall set by bedrock river incision and rock uplift. The potential feedbacks between intermittent sediment cover, soil production rates, nonlocal transport, and headwater channel incision in bedrock landscapes are essentially unknown.

Upscaling the particle-based approach presented here is challenging and requires a number of parameters that may be difficult to obtain for natural landscapes. Nonetheless, there are some potential avenues to incorporate these results more broadly. For example, the scaling of topographic variability with mean hillslope gradient is promising for parameterizing how roughness influences hillslope sediment transport at multiple scales. As topographic surveys increase in resolution (from ~1 to 10s of points or more per square meter), analysis of point cloud data directly will help upscale the insight gained from focused terrestrial surveys to whole landscapes. Additionally, vegetation mapping will help to quantify spatial and temporal changes in vegetation density and associated impacts on roughness.

**7 Conclusions**

Using a combination of hillslope-scale dry ravel experiments and a series of 1D and 2D numerical simulations, we documented the sensitivity of hillslope sediment transport to grain size, slope, and surface roughness characterized at two scales. In agreement with prior laboratory and field experiments, we showed that a modified sliding block model captures to first order the behavior of bouncing, rolling, and sliding associated with dry ravel transport on steep hillslopes. The sliding block model is most sensitive to the hillslope gradient normalized by the effective dynamic friction slope, the latter of which increases systematically with the ratio of topographic micro-roughness to particle size. In contrast to threshold models of hillslope sediment transport that assume a single critical slope (the friction slope) that delineates soil-mantled from bare-bedrock landscapes, the particle-based model assumes a variable friction slope that depends on roughness and grain size, resulting in a gradual transition from local to nonlocal transport across slope gradients one- to three-fold the friction slope due to the trapping of sediment on rough hillslopes. The ability for steep slopes to temporarily store sediment is enhanced (up to a factor of 3) by an increase in macro-topographic variability that accompanies an increase in bedrock exposure as hillslopes steepen. By expanding the 1D model to a new 2D ravel-routing model over high resolution topography, we showed the potential for particle-based models to highlight patterns of local and nonlocal sediment transport in landscapes.

Three key implications emerge from this study. First, for a given hillslope, transport distance, and thus sediment flux, increases with grain size, providing a framework for evaluating the grain-size dependence of hillslope-channel connectivity and coupling between hillslope sediment production and channel bed cover. Second, our 2D ravel-routing model highlights how pulses of sediment delivery from steep hillslopes, for example from vegetation burning during wildfire [*DiBiase and Lamb*, 2013], can be a significant source of

sediment to steep headwater channels. By quantifying the spatial patterns of channel sediment loading by dry ravel, our 2D model can help inform models of in-channel debris flow initiation [*Prancevic et al.*, 2014] necessary for building mechanistic models of post-wildfire sedimentation hazards. Third, the broad transition from local to purely nonlocal transport and stability of sediment on rough, steep hillslopes corroborate field observations of a gradual and patchy transition from soil-mantled to bedrock landscapes [*DiBiase et al.*, 2012] and suggests that there is a dynamic interplay between sediment storage, roughness, grain sorting, and soil transport even on hillslopes that well-exceed the angle of repose.

## Acknowledgments

## References

Andrews, D. J., and R. C. Bucknam (1987), Fitting degradation of shoreline scarps by a nonlinear diffusion model, *J. Geophys. Res. Solid Earth*, *92*(B12), 12857-12867, doi:10.1029/JB092iB12p12857

Attal, M., S. M. Mudd, M. D. Hurst, B. Weinman, K. Yoo, and M. Naylor (2015), Impact of change in erosion rate and landscape steepness on hillslope and fluvial sediments grain size in the Feather River basin (Sierra Nevada, California), *Earth Surf. Dynam.*, *3*(1), 201-222, doi:10.5194/esurf-3-201-2015

Batrouni, G. G., S. Dippel, and L. Samson (1996), Stochastic model for the motion of a particle on an inclined rough plane and the onset of viscous friction, *Phys. Rev. E*, *53*(6), 6496-6503, doi:10.1103/PhysRevE.53.6496

Benda, L., and T. Dunne (1997), Stochastic forcing of sediment supply to channel networks from landsliding and debris flow, *Water Resour. Res.*, *33*(12), 2849-2863, doi:10.1029/97WR02388

Bennett, G. L., P. Molnar, B. W. McArdell, and P. Burlando (2014), A probabilistic sediment cascade model of sediment transfer in the Illgraben, *Water Resour. Res.*, *50*(2), 1225-1244, doi:10.1002/2013wr013806

Bennett, K. A. (1982), Effects of slash burning on surface soil erosion rates in the Oregon Coast Range, M.S. Thesis, Oregon State University, Corvallis, OR.

Bourrier, F., F. Berger, P. Tardif, L. Dorren, and O. Hungr (2012), Rockfall rebound: comparison of detailed field experiments and alternative modelling approaches, *Earth Surf. Processes Landforms*, *37*(6), 656-665, doi:10.1002/esp.3202

Brasington, J., D. Vericat, and I. Rychkov (2012), Modeling river bed morphology, roughness, and surface sedimentology using high resolution terrestrial laser scanning, *Water Resour. Res.*, *48*(11), doi:10.1029/2012WR012223

Brummer, C. J., and D. R. Montgomery (2003), Downstream coarsening in headwater channels, *Water Resour. Res.*, *39*(10), doi: 10.1029/2003WR001981

Buffington, J. M., W. E. Dietrich, and J. W. Kirchner (1992), Friction angle measurements on a naturally formed gravel streambed: Implications for critical boundary shear stress, *Water Resour. Res.*, *28*(2), 411-425, doi:10.1029/91WR02529

Burbank, D. W., J. Leland, E. Fielding, R. S. Anderson, N. Brozovic, M. R. Reid, and C. Duncan (1996), Bedrock incision, rock uplift and threshold hillslopes in the northwestern Himalayas, *Nature*, *379*(6565), 505-510, doi:10.1038/379505a0

Cannon, S. H., J. E. Gartner, M. G. Rupert, J. A. Michael, A. H. Rea, and C. Parrett (2010), Predicting the probability and volume of postwildfire debris flows in the intermountain western United States, *Geol. Soc. Am. Bull.*, *122*(1-2), 127-144, doi:10.1130/b26459.1

DiBiase, R. A., and K. X. Whipple (2011), The influence of erosion thresholds and runoff variability on the relationships among topography, climate, and erosion rate, *J. Geophys. Res. Earth Surf.*, *116*, F04036, doi:10.1029/2011JF002095

DiBiase, R. A., and M. P. Lamb (2013), Vegetation and wildfire controls on sediment yield in bedrock landscapes, *Geophys. Res. Lett.*, *40*(6), 1093-1097, doi:10.1002/grl.50277

DiBiase, R. A., A. M. Heimsath, and K. X. Whipple (2012), Hillslope response to tectonic forcing in threshold landscapes, *Earth Surf. Processes Landforms*, *37*(8), 855-865, doi:10.1002/esp.3205

DiBiase, R. A., K. X. Whipple, A. M. Heimsath, W. B. Ouimet (2010), Landscape form and millennial erosion rates in the San Gabriel Mountains, CA, *Earth Planet. Sci. Lett.,* *289*, 134-144, doi:10.1016/j.espl.2009.10.036

Dietrich, W. E., D. G. Bellugi, L. S. Sklar, J. D. Stock, A. M. Heimsath, and J. J. Roering (2003), Geomorphic transport laws for predicting landscape form and dynamics, in *Prediction in Geomorphology*, edited, pp. 103-132, American Geophysical Union.

Dixon, J. L., A. S. Hartshorn, A. M. Heimsath, R. A. DiBiase, and K. X. Whipple (2012), Chemical weathering response to tectonic forcing: A soils perspective from the San Gabriel Mountains, California, *Earth Planet. Sci. Lett.*, *323–324*, 40-49, doi:10.1016/j.epsl.2012.01.010

Dorren, L. K. A., B. Maier, U. S. Putters, and A. C. Seijmonsbergen (2004), Combining field and modelling techniques to assess rockfall dynamics on a protection forest hillslope

in the European Alps, *Geomorphology*, *57*(3–4), 151-167, doi:10.1016/S0169-555X(03)00100-4

Ferrier, K. L., and J. W. Kirchner (2008), Effects of physical erosion on chemical denudation rates: A numerical modeling study of soil-mantled hillslopes, *Earth Planet. Sci. Lett.*, *272*(3–4), 591-599, doi:10.1016/j.epsl.2008.05.024

Florsheim, J. L., E. A. Keller, and D. W. Best (1991), Fluvial sediment transport in response to moderate storm flows following chaparral wildfire, Ventura County, southern California, *Geological Society of America Bulletin*, *103*(4), 504-511, doi:10.1130/0016-7606(1991)103<0504:fstirt>2.3.co;2

Foufoula-Georgiou, E., V. Ganti, and W. E. Dietrich (2010), A nonlocal theory of sediment transport on hillslopes, *J. Geophys. Res. Earth Surf.*, *115*(F2), doi:10.1029/2009JF001280

Furbish, D. J., and J. J. Roering (2013), Sediment disentrainment and the concept of local versus nonlocal transport on hillslopes, *J. Geophys. Res. Earth Surf.*, *118*(2), 937-952, doi:10.1002/jgrf.20071

Gabet, E. J. (2003), Sediment transport by dry ravel, *J. Geophys. Res. Solid Earth*, *108*(B1), doi:10.1029/2001JB001686

Gabet, E. J., and T. Dunne (2003), A stochastic sediment delivery model for a steep Mediterranean landscape, *Water Resour. Res.*, *39*(9), doi:10.1029/2003WR002341

Gabet, E. J., and M. K. Mendoza (2012), Particle transport over rough hillslope surfaces by dry ravel: Experiments and simulations with implications for nonlocal sediment flux, *J. Geophys. Res. Earth Surf.*, *117*(F1), doi:10.1029/2011JF002229

Ganti, V., P. Passalacqua, and E. Foufoula-Georgiou (2012), A sub-grid scale closure for nonlinear hillslope sediment transport models, *J. Geophys. Res. Earth Surf.*, *117*(F2), doi:10.1029/2011JF002181

Ganti, V., M. P. Lamb, and B. McElroy (2014), Quantitative bounds on morphodynamics and implications for reading the sedimentary record, *Nat. Commun.*, *5*, doi:10.1038/ncomms4298

Hack, J. T. (1957), Studies of longitudinal stream profiles in Virginia and Maryland, *U.S. Geol. Surv. Prof. Pap.*, *294-B*, 97 pp.

Heckmann, T., and W. Schwanghart (2013), Geomorphic coupling and sediment connectivity in an alpine catchment — Exploring sediment cascades using graph theory, *Geomorphology*, *182*, 89-103, doi:10.1016/j.geomorph.2012.10.033

Heimsath, A. M., R. A. DiBiase, and K. X. Whipple (2012), Soil production limits and the transition to bedrock dominated landscapes, *Nat. Geosci.*, *5*(3), 210-214, doi:10.1038/ngeo1380

Hilley, G. E., C. P. Chamberlain, S. Moon, S. Porder, and S. D. Willett (2010), Competition between erosion and reaction kinetics in controlling silicate-weathering rates, *Earth Planet. Sci. Lett.*, *293*(1–2), 191-199, doi:10.1016/j.epsl.2010.01.008

Howard, A. D., W. E. Dietrich, and M. A. Seidl (1994), Modeling fluvial erosion on regional to continental scales, *J. Geophys. Res. Solid Earth*, *99*(B7), 13971-13986, doi:10.1029/94JB00744

Jackson, M., and J. J. Roering (2009), Post-fire geomorphic response in steep, forested landscapes: Oregon Coast Range, USA, *Quaternary Science Reviews*, *28*(11–12), 1131-1146, doi:10.1016/j.quascirev.2008.05.003

Kean, J. W., D. M. Staley, and S. H. Cannon (2011), In situ measurements of post-fire debris flows in southern California: Comparisons of the timing and magnitude of 24 debris-flow events with rainfall and soil moisture conditions, *J. Geophys. Res. Earth Surf.*, *116*(F4), doi:10.1029/2011JF002005

Kean, J. W., S. W. McCoy, G. E. Tucker, D. M. Staley, and J. A. Coe (2013), Runoff-generated debris flows: Observations and modeling of surge initiation, magnitude, and frequency, *J. Geophys. Res. Earth Surf.*, *118*(4), 2190-2207, doi:10.1002/jgrf.20148

Kirchner, J. W., W. E. Dietrich, F. Iseya, and H. Ikeda (1990), The variability of critical shear stress, friction angle, and grain protrusion in water-worked sediments, *Sedimentology*, *37*(4), 647-672, doi:10.1111/j.1365-3091.1990.tb00627.x

Kirkby, M. J., and I. Statham (1975), Surface Stone Movement and Scree Formation, *J. Geol.*, *83*(3), 349-362, doi:10.2307/30059027

Lamb, M. P., M. Levina, R. A. DiBiase, and B. M. Fuller (2013), Sediment storage by vegetation in steep bedrock landscapes: Theory, experiments, and implications for postfire sediment yield, *J. Geophys. Res. Earth Surf.*, *118*(2), 1147-1160, doi:10.1002/jgrf.20058

Lamb, M. P., J. S. Scheingross, W. H. Amidon, E. Swanson, and A. Limaye (2011), A model for fire-induced sediment yield by dry ravel in steep landscapes, *J. Geophys. Res. Earth Surf.*, *116*(F3), doi:10.1029/2010JF001878

Larsen, I. J., P. C. Almond, A. Eger, J. O. Stone, D. R. Montgomery, and B. Malcolm (2014), Rapid Soil Production and Weathering in the Southern Alps, New Zealand, *Science*, *343*(6171), 637-640, doi:10.1126/science.1244908

Lavé, J. and D. Burbank (2004), Denudation processes and rates in the Transverse Ranges, southern California: Erosional response of a transitional landscape to external and anthropogenic forcing, *J. Geophys. Res. Earth Surf.*, *109*, F01006, doi:10.1029/2003JF000023

McKean, J., and J. Roering (2004), Objective landslide detection and surface morphology mapping using high-resolution airborne laser altimetry, *Geomorphology*, *57*(3–4), 331-351, doi:10.1016/S0169-555X(03)00164-8

Meyer, G. A., and S. G. Wells (1997), Fire-related sedimentation events on alluvial fans, Yellowstone National Park, USA, *J. Sediment. Res.*, *67*, 776-791, doi:10.1306/D426863A-2B26-11D7-8648000102C1865D

Miller, R. L., and R. J. Byrne (1966), The angle of repose for a single grain on a fixed rough bed, *Sedimentology*, *6*(4), 303-314, doi:10.1111/j.1365-3091.1966.tb01897.x

Milodowski, D. T., S. M. Mudd, and E. T. A. Mitchard (2015), Topographic roughness as a signature of the emergence of bedrock in eroding landscapes, *Earth Surf. Dynam.*, *3*(4), 483-499, doi:10.5194/esurf-3-483-2015

Montgomery, D. R., and M. T. Brandon (2002), Topographic controls on erosion rates in tectonically active mountain ranges, *Earth Planet. Sci. Lett.*, *201*(3–4), 481-489, doi:10.1016/S0012-821X(02)00725-2

Nikora, V. I., D. G. Goring, and B. J. Biggs (1998), On gravel-bed roughness characterization, *Water Resour. Res.*, *34*, 517-527, doi: 10.1029/97WR02886

Norton, K. P., F. von Blanckenburg, and P. W. Kubik (2010), Cosmogenic nuclide-derived rates of diffusive and episodic erosion in the glacially sculpted upper Rhone Valley, Swiss Alps, *Earth Surf. Processes Landforms*, *35*(6), 651-662, doi:10.1002/esp.1961

Petley, D. (2012), Global patterns of loss of life from landslides, *Geology*, *40*(10), 927-930, doi:10.1130/g33217.1

Pollyea, R. M., and J. P. Fairley (2011), Estimating surface roughness of terrestrial laser scan data using orthogonal distance regression, *Geology*, *39*(7), 623-626, doi:10.1130/g32078.1

Prancevic, J. P., and M. P. Lamb (2015), Particle friction angles in steep mountain channels, *J. Geophys. Res. Earth Surf.*, *120*(2), 242-259, doi:10.1002/2014jf003286

Prancevic, J. P., M. P. Lamb, and B. M. Fuller (2014), Incipient sediment motion across the river to debris-flow transition, *Geology*, *42*(3), 191-194, doi:10.1130/g34927.1

Quartier, L., B. Andreotti, S. Douady, and A. Daerr (2000), Dynamics of a grain on a sandpile model, *Phys. Rev. E*, *62*(6), 8299-8307

Rapp, A. (1960), Recent development of mountain slopes in Karkevagge and surroundings, Northern Scandinavia, *Geografiska Annaler*, *42*(2/3), 65-200, doi:10.2307/520126

Reneau, S. L., and W. E. Dietrich (1987), The importance of hollows in debris flow studies; Examples from Marin County, California, *Reviews in Engineering Geology*, *7*, 165-180, doi:10.1130/REG7-p165

Riebe, C. S., L. S. Sklar, C. E. Lukens, and D. L. Shuster (2015), Climate and topography control the size and flux of sediment produced on steep mountain slopes, *Proc. Natl. Acad. Sci. U. S. A.*, *112*(51), 15574-15579, doi:10.1073/pnas.1503567112

Roering, J. J. (2008), How well can hillslope evolution models "explain" topography? Simulating soil transport and production with high-resolution topographic data, *Geol. Soc. Am. Bull.*, *120*, 1248-1262, doi:10.1130/B26283.1

Roering, J. J., and M. Gerber (2005), Fire and the evolution of steep, soil-mantled landscapes, *Geology*, *33*(5), 349-352, doi:10.1130/g21260.1

Roering, J. J., J. W. Kirchner, and W. E. Dietrich (1999), Evidence for nonlinear, diffusive sediment transport on hillslopes and implications for landscape morphology, *Water Resour. Res.*, *35*(3), 853-870, doi:10.1029/1998WR900090

Roering, J. J., J. Marshall, A. M. Booth, M. Mort, and Q. Jin (2010), Evidence for biotic controls on topography and soil production, *Earth Planet. Sci. Lett.*, *298*(1–2), 183-190, doi:10.1016/j.epsl.2010.07.040

Schmidt, K. M., and D. R. Montgomery (1995), Limits to relief, *Science*, *270*(5236), 617-620

Schumer, R., Meerschaert, M. M., and B. Baeumer (2009), Fractional advection-dispersion equations for modeling transport at the Earth surface, *J. Geophys. Res. Earth Surf.*, *114*(F4), doi:10.1029/2008JF001246

Sklar, L. S., and W. E. Dietrich (2004), A mechanistic model for river incision into bedrock by saltating bed load, *Water Resour. Res.*, *40*(6), doi:10.1029/2003wr002496

Sklar, L. S., and W. E. Dietrich (2006), The role of sediment in controlling steady-state bedrock channel slope: Implications of the saltation–abrasion incision model, *Geomorphology*, *82*(1-2), 58-83, doi:10.1016/j.geomorph.2005.08.019

Smith, M. W. (2014), Roughness in the earth sciences, *Earth-Sci. Rev. 136*, 202-225, doi:10.1016/j.earscirev.2014.05.016

Statham, I. (1976), A scree slope rockfall model, *Earth Surf. Processes*, *1*(1), 43-62, doi:10.1002/esp.3290010106

Takahashi, T. (1978), Mechanical characteristics of debris flow, *J. Hydraul. Div., Am. Soc. Civ. Eng.*, *104*(8), 1153-1169

Tucker, G. E., and D. N. Bradley (2010), Trouble with diffusion: Reassessing hillslope erosion laws with a particle-based model, *J. Geophys. Res. Earth Surf.*, *115*(F1), doi:10.1029/2009JF001264

Tucker, G. E., and G. R. Hancock (2010), Modelling landscape evolution, *Earth Surf. Processes Landforms*, *35*(1), 28-50, doi:10.1002/esp.1952

Wells, W. G. (1987), The effects of fire on the generation of debris flows in southern California, *Rev. Eng. Geol.*, *7*, 105-114, doi:10.1130/REG7-p105

West, A. J. (2012), Thickness of the chemical weathering zone and implications for erosional and climatic drivers of weathering and for carbon-cycle feedbacks, *Geology*, *40*(9), 811-814, doi:10.1130/g33041.1

Wiberg, P. L., and J. D. Smith (1987), Calculations of the critical shear stress for motion of uniform and heterogeneous sediments, *Water Resour. Res.*, *23*(8), 1471-1480, doi:10.1029/WR023i008p01471
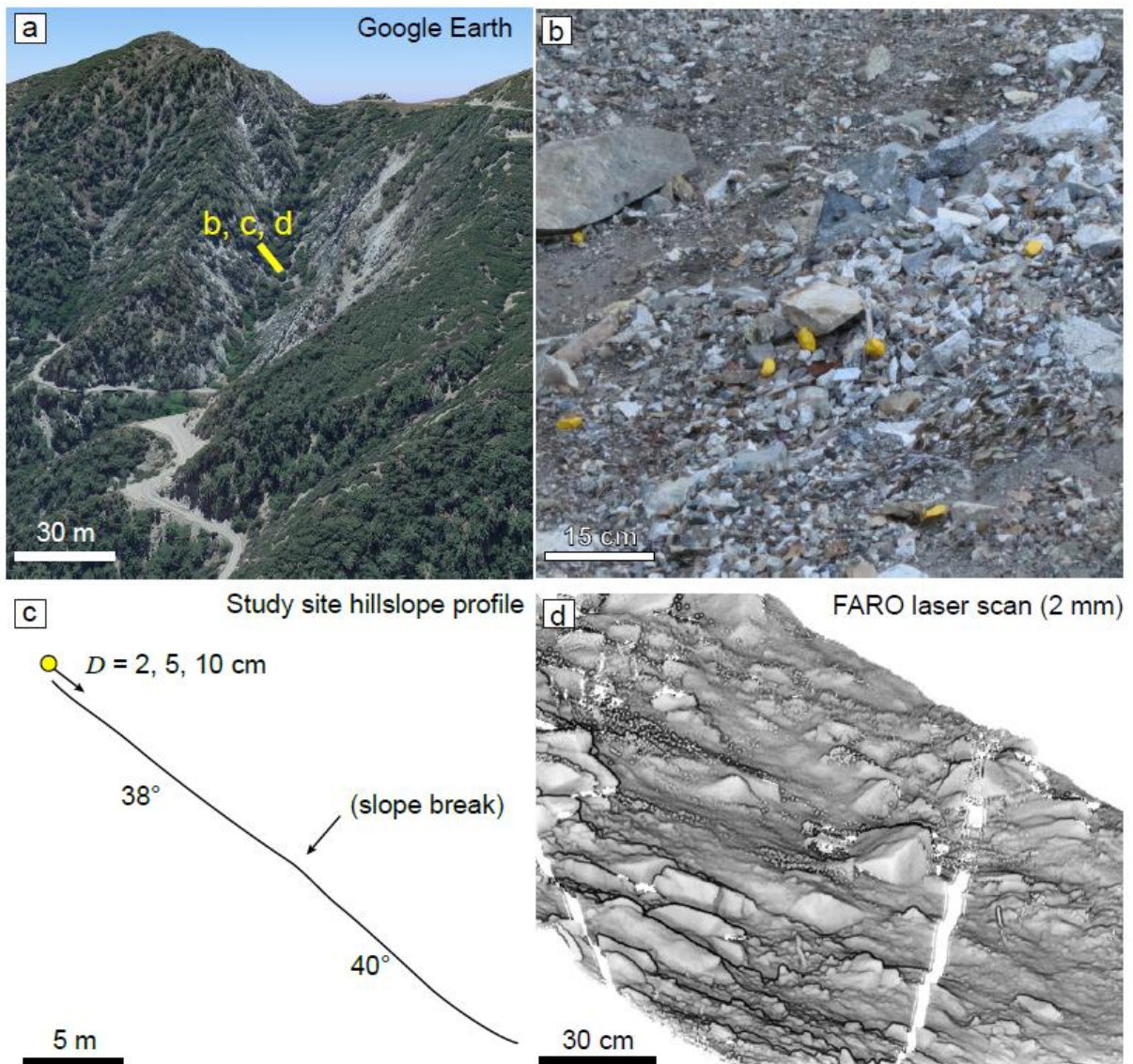
**Figure 1.** Overview of experimental hillslope and study area, showing **a)** location of hillslope in the San Gabriel Mountains, CA (looking south to yellow line, 34.2479°N, 118.1010°W), **b)** photograph of surface cover on study hillslope including 2-3 cm diameter tracer particles, **c)** schematic of study hillslope, and **d)** shaded point cloud derived from high-resolution terrestrial laser scan of hillslope (2 mm point spacing).
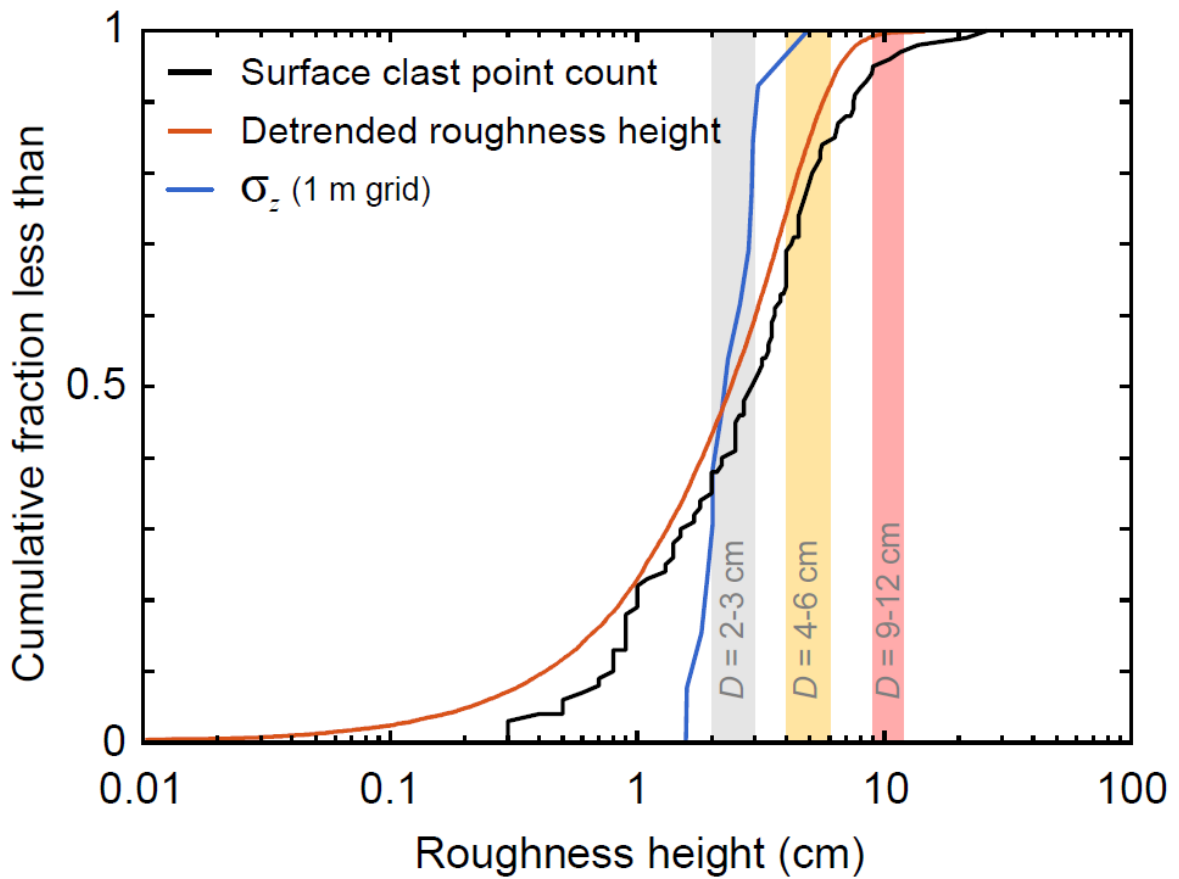
**Figure 2.** Cumulative distribution plots of surface roughness estimates for study hillslope, showing results from surface point count (black line), detrended roughness height determined from laser scan of hillslope (red line), and the standard deviation of roughness height $\sigma_z$ for each 1 m x 1 m cell across the experimental hillslope (blue line). Shaded vertical bars indicate size classes for particles used in hillslope experiments.
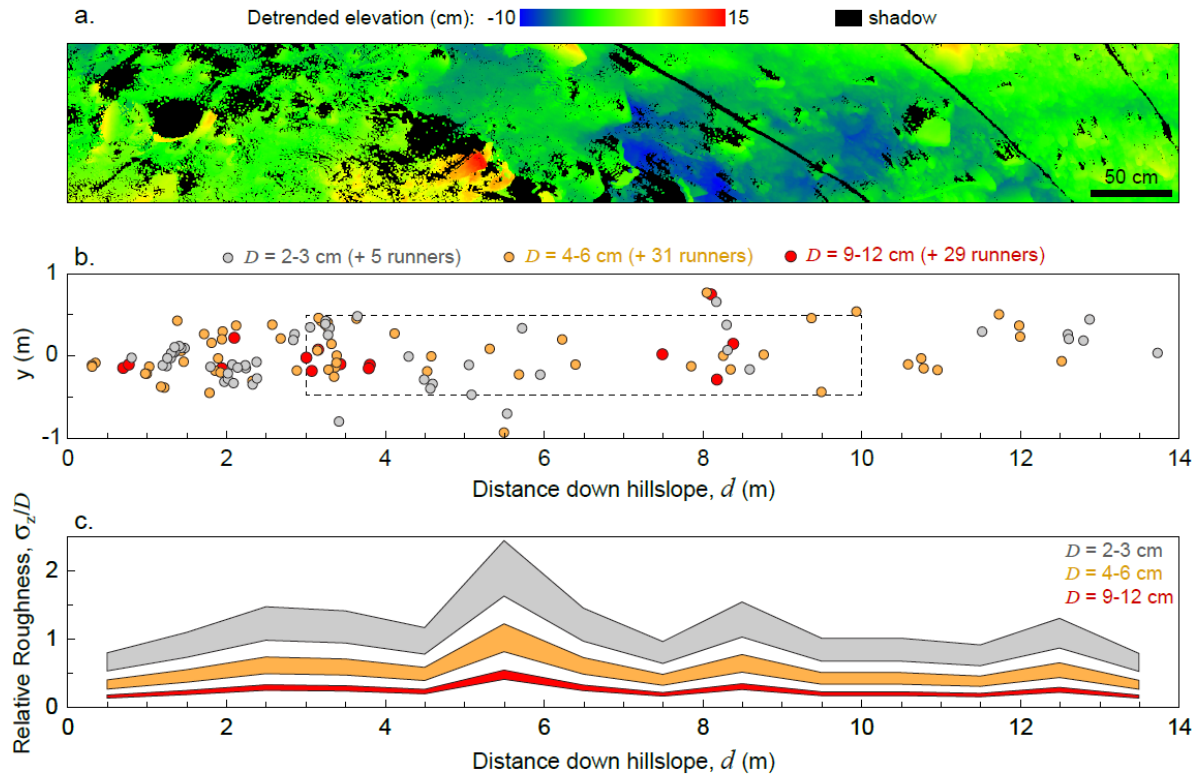
**Figure 3.** Map of hillslope ravel experimental results, showing **a)** spatial patterns in detrended elevation determined from laser scan (extent given by dashed box in **b)**; **b)** map-view distribution of final particle locations as measured from laser rangefinder; and **c)** longitudinal patterns in relative roughness based on the normalized roughness metric $\sigma_z/D$ (thickness in bar represents variation in $D$ for each size class). For all panels, view is normal to the hillslope surface.
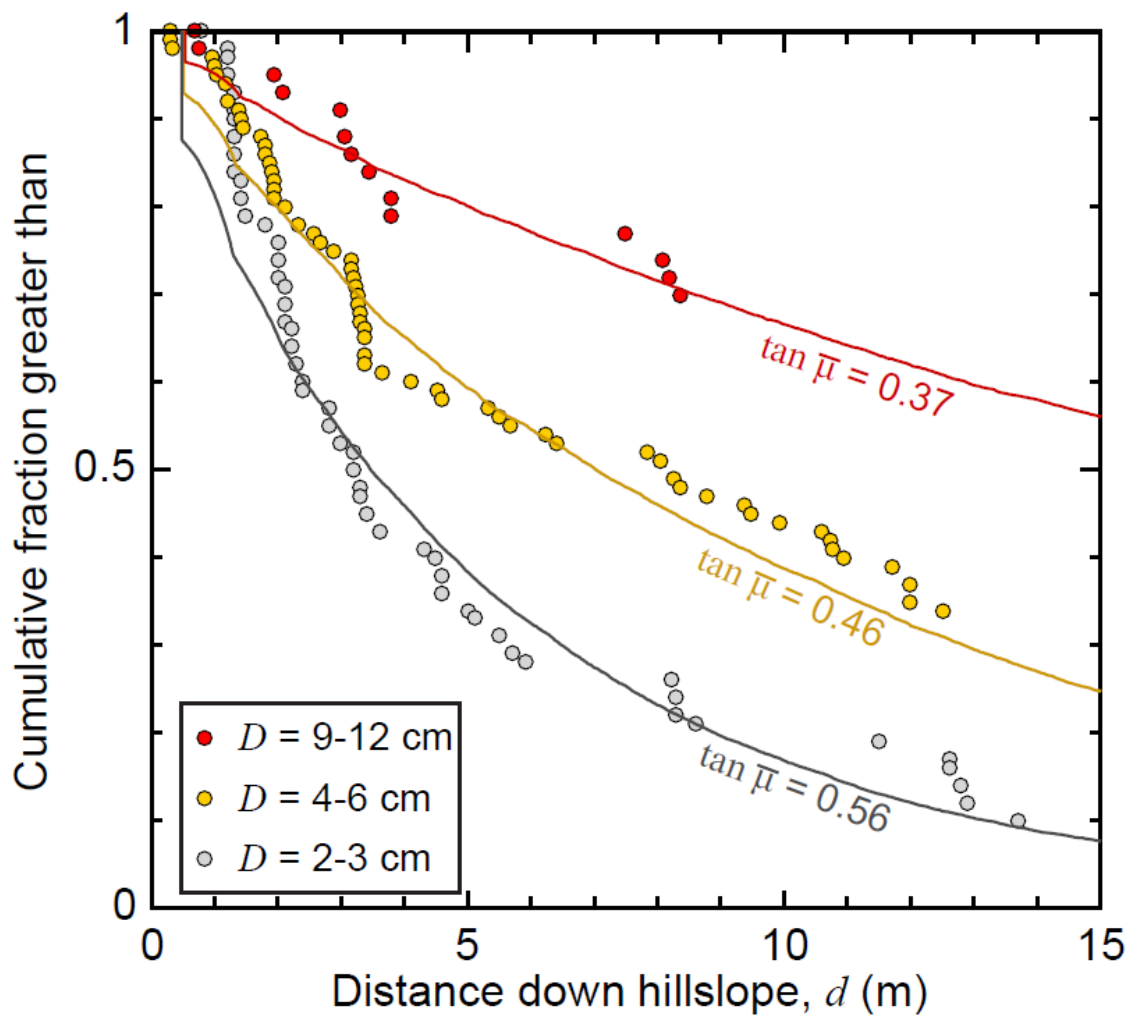
**Figure 4.** Cumulative distribution plot of particle travel distances from hillslope experiments, with numerical simulations from Section 4.3 shown by solid lines. Model parameters provided in Table 2.
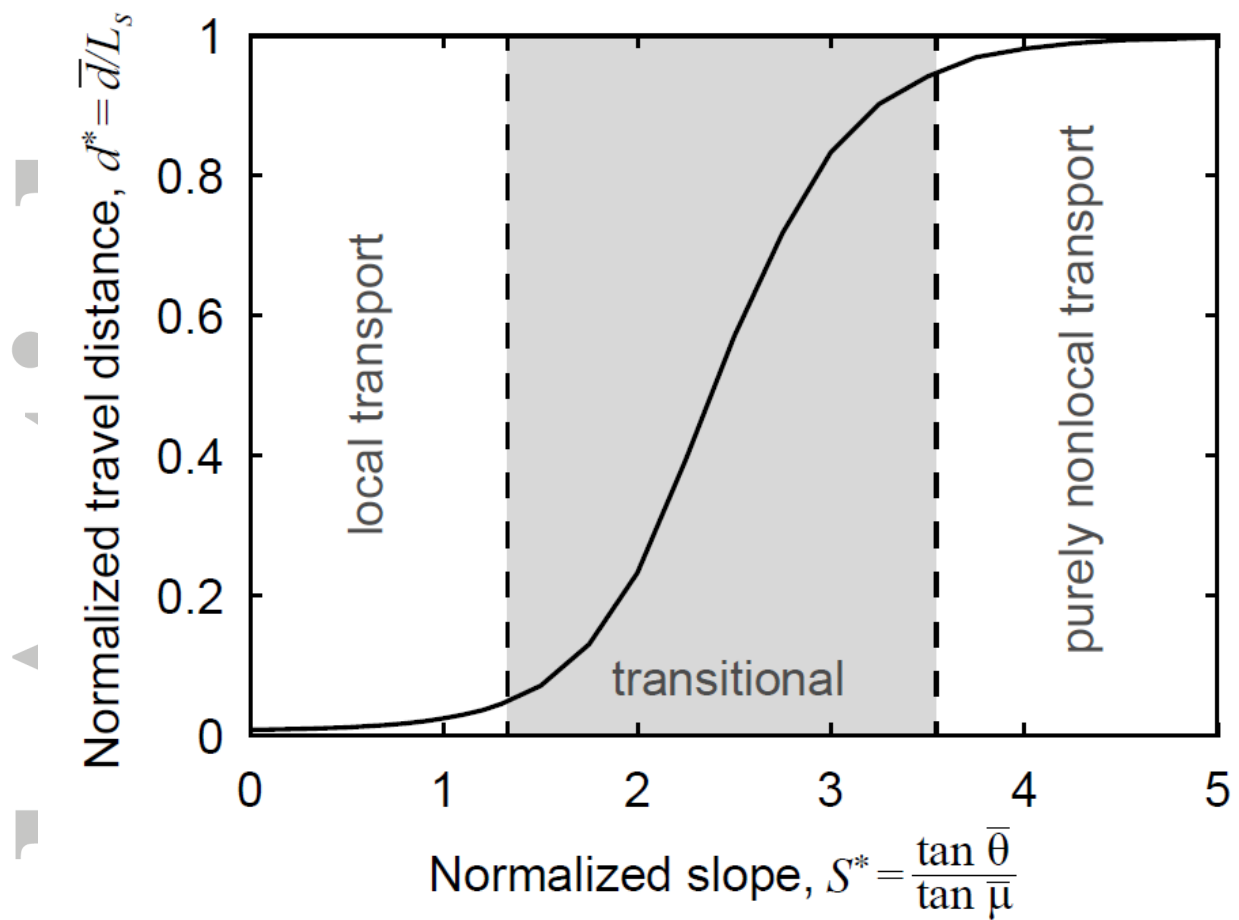
**Figure 5.** Plot of normalized travel distance versus normalized slope for the baseline, 1D smooth hillslope model, highlighting broad transition from local ($d^* < 0.05$) to purely nonlocal ($d^* > 0.95$) transport. Model parameters provided in Table 2.
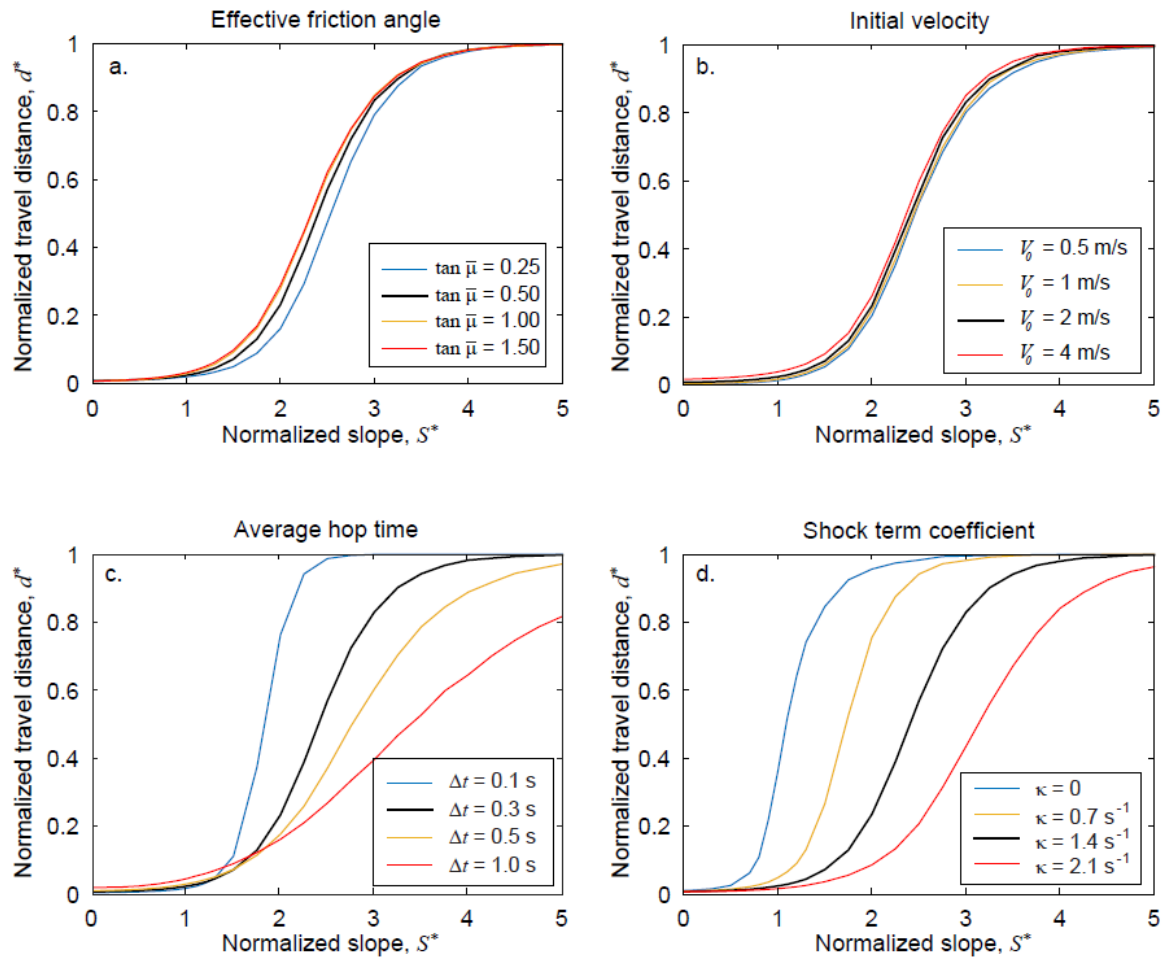
**Figure 6.** Sensitivity analysis for 1D smooth hillslope model, showing the relationship between normalized travel distance and normalized slope with varying **a)** mean effective friction slope; **b)** initial velocity; **c)** mean hop time; and **d)** shock term coefficient. For all cases, baseline model run (Figure 5) is shown for reference in black. Model parameters for all runs provided in Table 2.
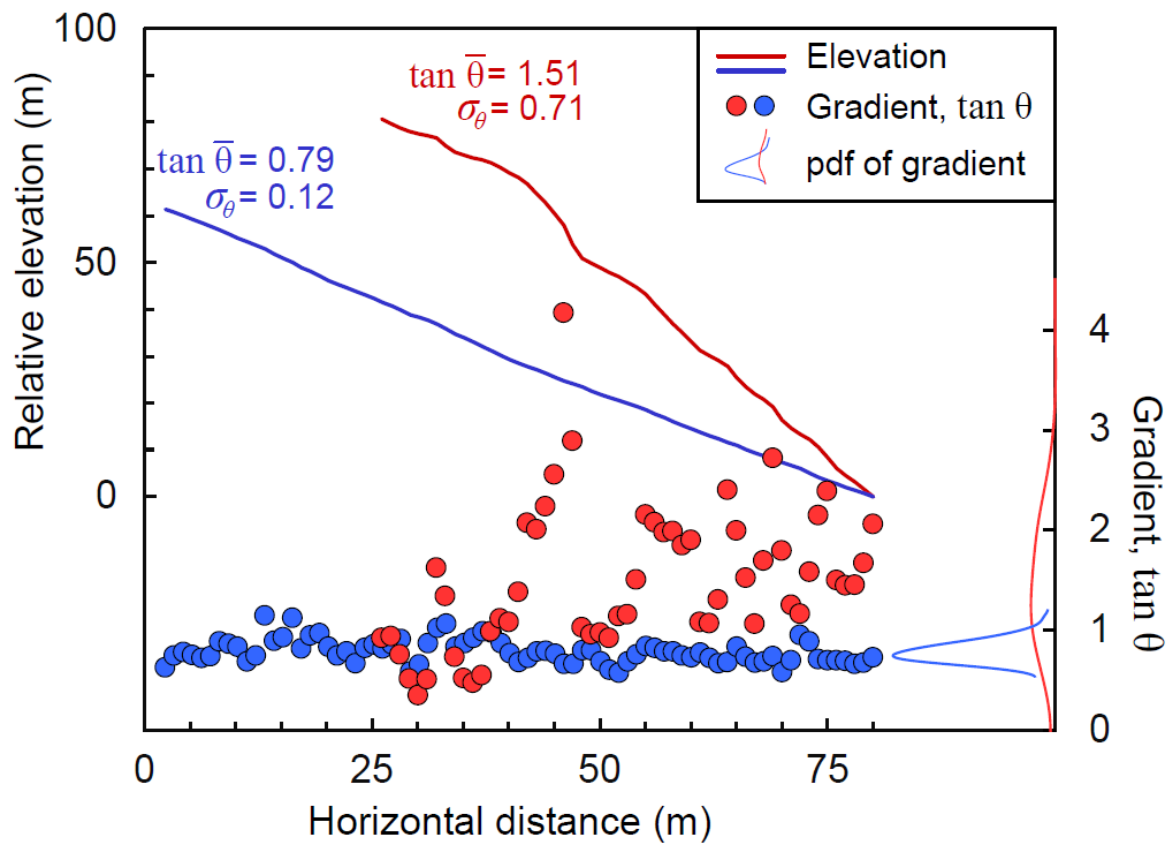
**Figure 7.** Comparison of two contrasting hillslopes from the San Gabriel Mountains, in the vicinity of Figure 1a, showing profiles of elevation (solid lines) and local hillslope gradient (circles). Probability density functions of local hillslope gradient for each profile are shown using kernel density estimation to visualize macro-topographic variability, which we define using the standard deviation of slope gradient, $\sigma_\theta$.
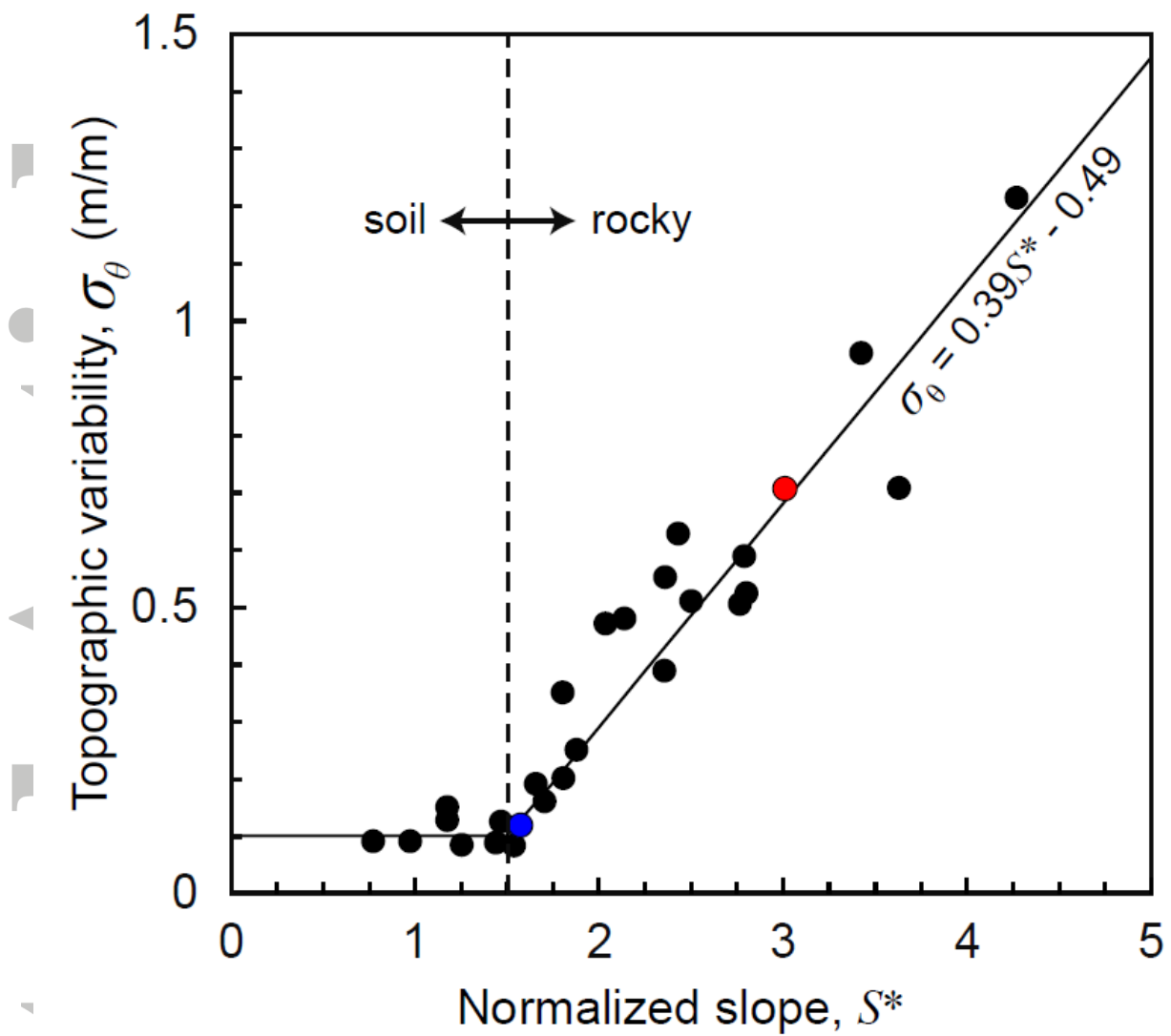
**Figure 8.** Plot of the topographic variability parameter, $\sigma_\theta$, as a function of average normalized hillslope gradient for 28 1D hillslope profiles measured in the vicinity of Figure 1a, including the two examples shown in Figure 7 indicated by the blue and red points. Solid line indicates piece-wise linear function used for model application in Figure 9.
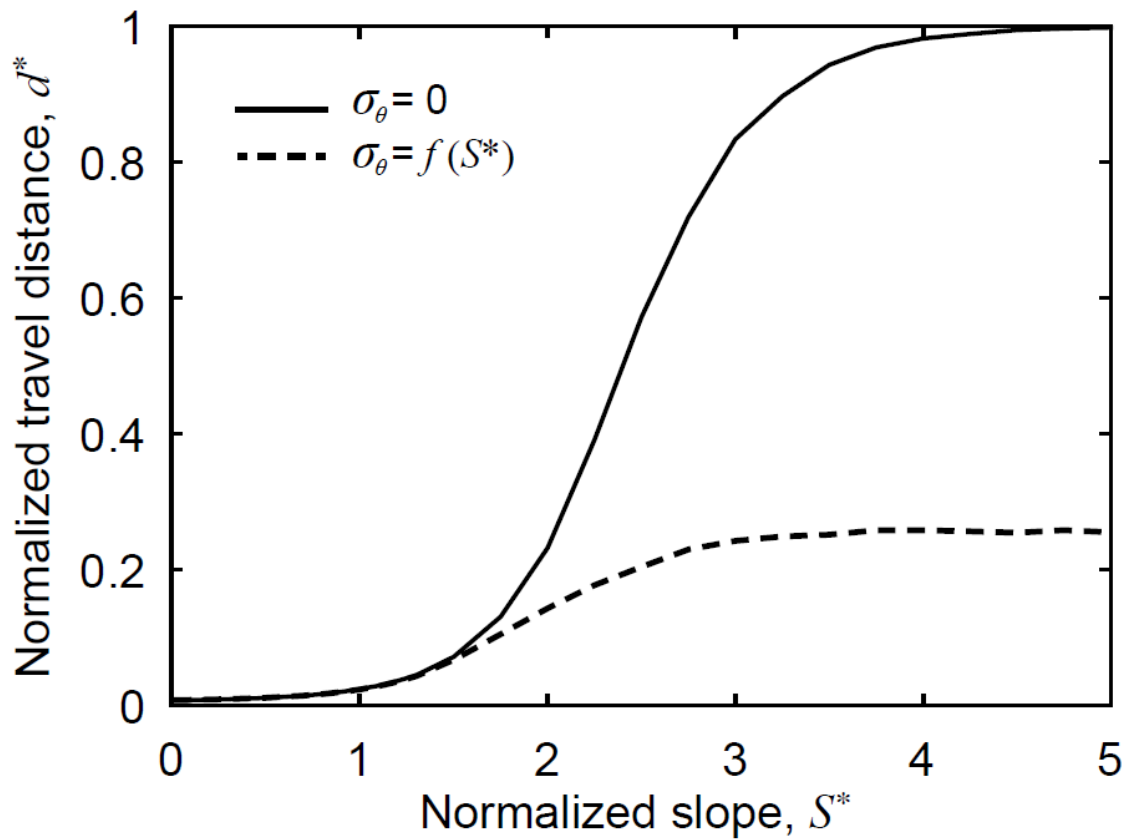
**Figure 9.** Comparison of 1D smooth hillslope model (Figure 5) and a 1D rough hillslope model incorporating increasing $\sigma_\theta$ as a function of normalized slope $S^*$. Normalized travel distance decreases by 60-75% for steep hillslopes, due to increased macro-topographic variability (Figure 8). Model parameters provided in Table 2.
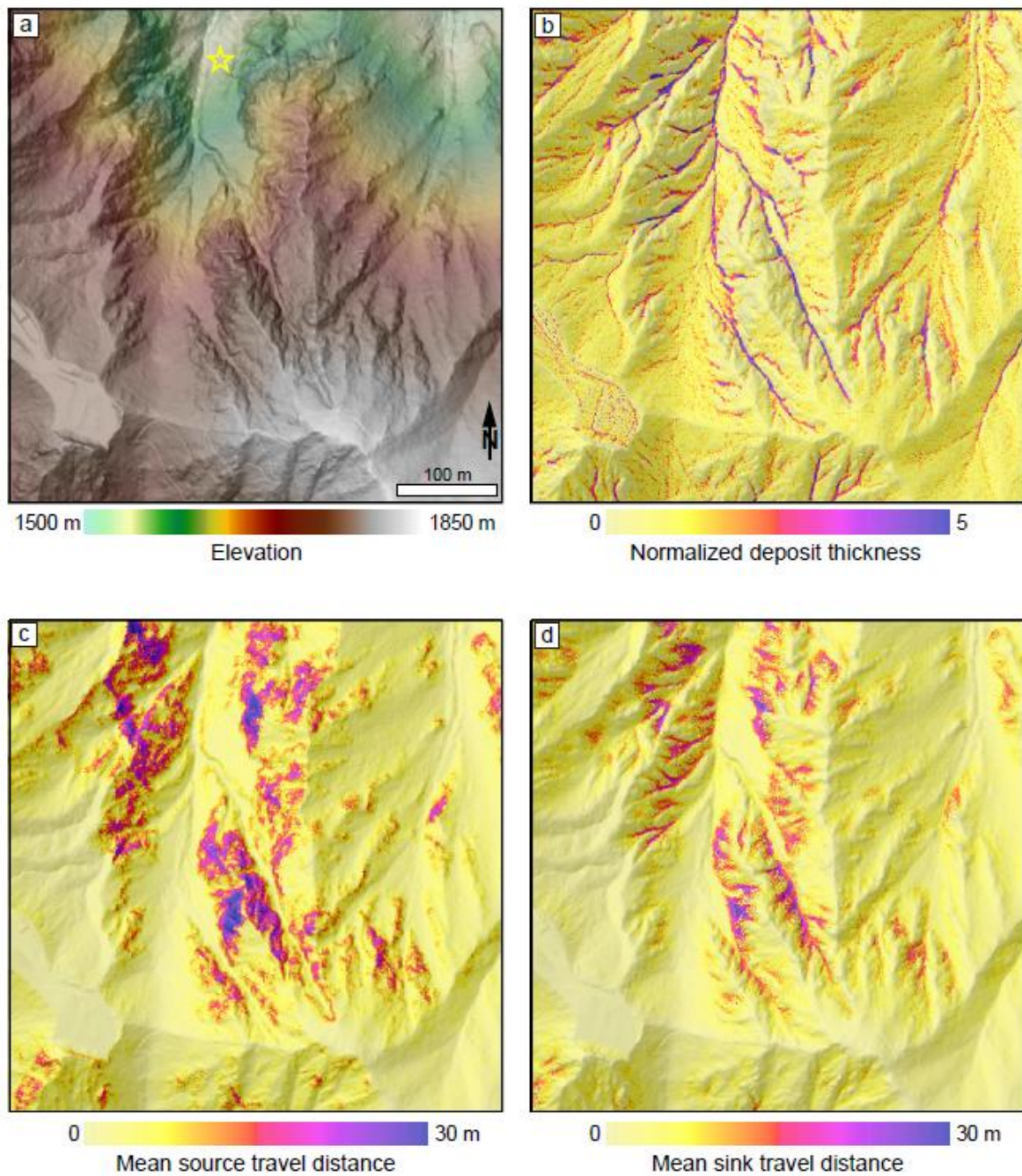
**Figure 10.** Results from 2D ravel routing model, showing **a)** topography of model domain in relation to location of hillslope experiments (star); **b)** normalized deposit thickness (total number of deposited particles divided by number of particles released per cell); **c)** mean particle travel distance for particles sourced from each cell; and **d)** mean particle travel distance for particles deposited at each cell. Model parameters provided in Table 2. Linear

stretch color map for panels **b)**, **c)**, and **d)** are clipped for clarity—maximum values for normalized deposit thickness (17), mean source travel distance (48 m), and mean sink travel distance (52 m) are not shown.
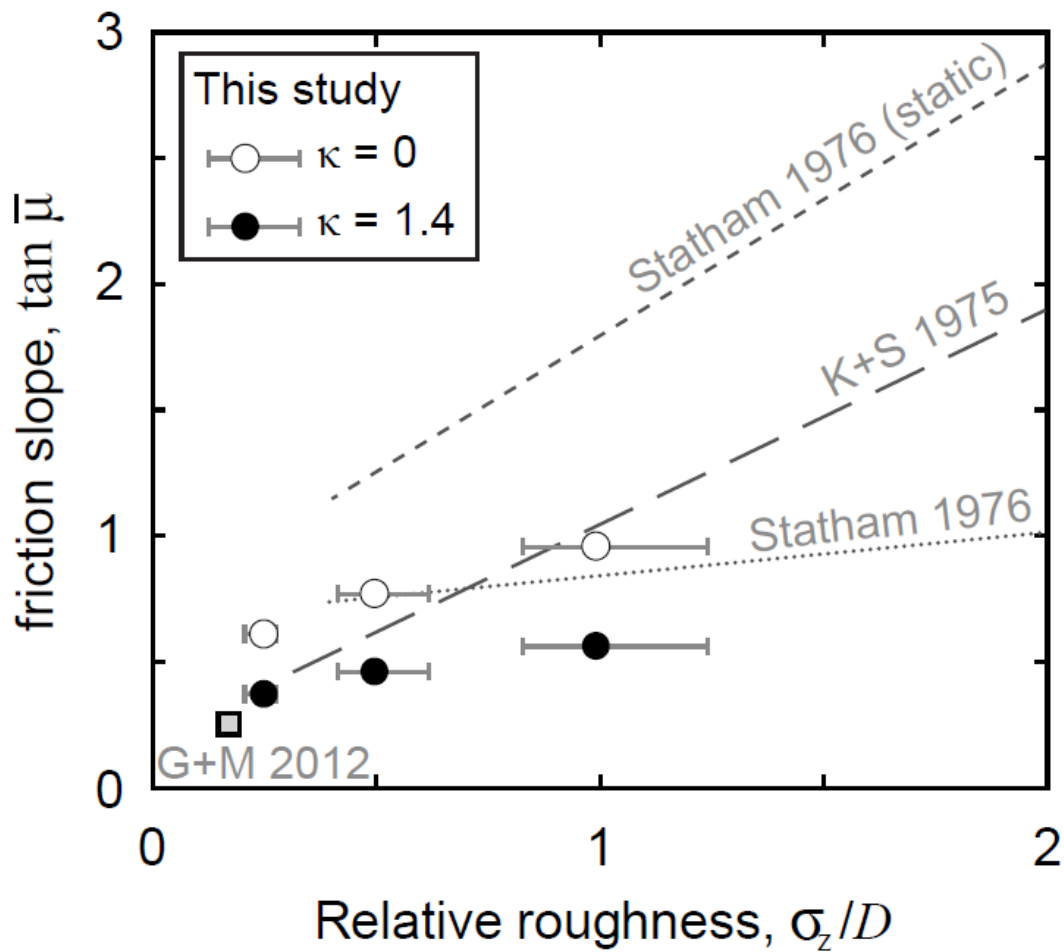
**Figure 11.** Plot of effective friction slope versus relative roughness for this study (circles), showing comparison to prior field and laboratory experiments. Solid circles indicate friction slopes calculated from simulations with $\kappa = 1.4$ s$^{-1}$ (Figure 4), while open circles indicate friction slopes calculated assuming $\kappa = 0$ (Supporting Information Figure S4) for comparison with sliding block model of *Kirkby and Statham* [1975] and *Statham* [1976]. Square symbol indicates laboratory measurement of dynamic effective friction slope by *Gabet and Mendoza* [2012]. Dotted line indicates trend of field experiments of dynamic effective friction slope by *Statham* [1976]. Long dashed line indicates laboratory dynamic friction slope from experiments of *Kirkby and Statham* [1975]. Short-dashed line indicates in-situ static friction slope measurements by *Statham* [1976].

**Table 1.** Parameters from field experiments and model fits to experimental data (Figure 4).

| | $D = 2$ cm | $D = 5$ cm | $D = 10$ cm |
|---|---|---|---|
| Number of particles | 58 | 93 | 43 |
| Particle diameter range[a] | 2-3 cm | 4-6 cm | 9-12 cm |
| Relative roughness, $\sigma_z/D$ | 0.9-1.3 | 0.4-0.6 | 0.2-0.3 |
| Initial velocity, $V_0$ | $1.6 \pm 0.2$[b] m/s | $1.8 \pm 0.2$ m/s | $1.8 \pm 0.2$ m/s |
| Mean $V_{mean}$[c] | $1.4 \pm 0.5$ m/s | $1.8 \pm 0.6$ m/s | $2.9 \pm 0.9$ m/s |
| Max $V_{mean}$ | 2.7 m/s | 3.3 m/s | 5.2 m/s |
| Fraction of runners | 0.09 | 0.33 | 0.67 |
| Model $\tan\overline{\mu}$ | 0.56 | 0.46 | 0.37 |
| Model mean $V_{mean}$ | 1.8 m/s | 2.1 m/s | 2.4 m/s |
| Model max $V_{mean}$ | 3.3 m/s | 3.3 m/s | 3.6 m/s |

[a] Intermediate axis diameter

[b] Uncertainty on velocity measurements reflects $\pm 1$ standard deviation (See Supporting Information Table S1)

[c] For runners, Vmean calculated only for first 14 m of travel distance

**Table 2.** Input parameters used for numerical experiments.

| Scenario | Figure | $n^a$ | $\tan\overline{\mu}$ | $V_0$ | $\Delta t$ | $\kappa$ | $\sigma_\theta$ |
|---|---|---|---|---|---|---|---|
| Field experiments | Fig. 4 | $1 \times 10^4$ | varies | varies | 0.3 s | 1.4 s$^{-1}$ | 0 |
| 1D smooth hillslope | Fig. 5 | $1 \times 10^4$ | 0.5 | 2 m/s | 0.3 s | 1.4 s$^{-1}$ | 0 |
| 1D smooth hillslope | Fig. 6a | $1 \times 10^4$ | varies | 2 m/s | 0.3 s | 1.4 s$^{-1}$ | 0 |
| 1D smooth hillslope | Fig. 6b | $1 \times 10^4$ | 0.5 | varies | 0.3 s | 1.4 s$^{-1}$ | 0 |
| 1D smooth hillslope | Fig. 6c | $1 \times 10^4$ | 0.5 | 2 m/s | varies | 1.4 s$^{-1}$ | 0 |
| 1D smooth hillslope | Fig. 6d | $1 \times 10^4$ | 0.5 | 2 m/s | 0.3 s | varies | 0 |
| 1D rough hillslope | Fig. 9 | $1 \times 10^4$ | 0.5 | 2 m/s | 0.3 s | 1.4 s$^{-1}$ | Figure 8 |
| 2D ravel routing | Fig. 10 | $5 \times 10^6$ | 0.5 | 2 m/s | 0.3 s | 1.4 s$^{-1}$ | from topography |

[a] Number of particles simulated